CrossMark

C A M B R I D G E
UNIVERSITY PRESS

Research Article

GaLactic and Extragalactic All-sky Murchison Widefield Array survey eXtended (GLEAM-X) I: Survey description and initial data release

N. Hurley-Walker[1], T. J. Galvin[1,2], S. W. Duchesne[1,2], X. Zhang[2,3], J. Morgan[1], P. J. Hancock[1,4], T. An[3], T. M. O. Franzen[5], G. Heald[2], K. Ross[1], T. Vernstrom[2,6], G. E. Anderson[1], B. M. Gaensler[7], M. Johnston-Hollitt[4], D. L. Kaplan[8], C. J. Riseley[2,9,10], S. J. Tingay[1], and M. Walker[1]

[1]International Centre for Radio Astronomy Research, Curtin University, Bentley, WA 6102, Australia, [2]CSIRO Space & Astronomy, PO Box 1130, Bentley, WA 6102, Australia, [3]Shanghai Astronomical Observatory, Chinese Academy of Sciences, 80 Nandan Rd, Shanghai 200030, China, [4]Curtin Institute for Computation, Curtin University, GPO Box U1987, Perth, WA 6845, Australia, [5]ASTRON, Netherlands Institute for Radio Astronomy, Oude Hoogeveensedijk 4, PD 7991, Dwingeloo, The Netherlands, [6]International Centre for Radio Astronomy Research, The University of Western Australia, 35 Stirling Hwy, 6009 Crawley, Australia, [7]Dunlap Institute for Astronomy and Astrophysics, 50 St. George St, University of Toronto, ON M5S 3H4, Canada, [8]Department of Physics, University of Wisconsin–Milwaukee, Milwaukee, WI 53201, USA, [9]Dipartimento di Fisica e Astronomia, Università degli Studi di Bologna, via P. Gobetti 93/2, 40129 Bologna, Italy and [10]INAF – Istituto di Radioastronomia, via P. Gobetti 101, 40129 Bologna, Italy

Abstract

We describe a new low-frequency wideband radio survey of the southern sky. Observations covering 72–231 MHz and Declinations south of $+30°$ have been performed with the Murchison Widefield Array "extended" Phase II configuration over 2018–2020 and will be processed to form data products including continuum and polarisation images and mosaics, multi-frequency catalogues, transient search data, and ionospheric measurements. From a pilot field described in this work, we publish an initial data release covering $1{,}447 \deg^2$ over $4\,\mathrm{h} \le \mathrm{RA} \le 13\,\mathrm{h}$, $-32.7° \le \mathrm{Dec} \le -20.7°$. We process twenty frequency bands sampling 72–231 MHz, with a resolution of $2'–45''$, and produce a wideband source-finding image across 170–231 MHz with a root mean square noise of 1.27 ± 0.15 mJy beam^{-1}. Source-finding yields 78,967 components, of which 71,320 are fitted spectrally. The catalogue has a completeness of 98% at $\sim$50 mJy, and a reliability of 98.2% at 5σ rising to 99.7% at 7σ. A catalogue is available from Vizier; images are made available via the PASA datastore, AAO Data Central, and SkyView. This is the first in a series of data releases from the GLEAM-X survey.

Keywords: techniques: interferometric – galaxies: general – radio continuum: surveys

(Received 22 February 2022; revised 30 March 2022; accepted 1 April 2022)

1. Introduction

Radio sky surveys offer a view of the high-energy sky, probing synchrotron, cyclotron, and thermal processes across a range of distances, from planets and exoplanets to high-redshift radio galaxies. At lower frequencies, the fields of view of radio telescopes are larger, enabling large-scale surveys of the radio sky, such as the National Radio Astronomy Observatory (NRAO) Very Large Array (VLA) Sky Survey (NVSS; Condon et al. 1998) at 1.4 GHz, the Sydney University Molonglo Sky Survey (SUMSS; Bock, Large, & Sadler 1999; Mauch et al. 2003), and the Low-frequency Sky Survey Redux at 74 MHz (VLSSr; Lane et al. 2014). Spurred by the development of the Square Kilometre Array (SKA), new radio telescopes are exploring the radio sky across wider areas and frequency ranges than accessible in the past (Figure 1).

The Murchison Widefield Array (MWA; Tingay et al. 2013), operational since 2013, is a precursor to the low-frequency component of the SKA, which will be the world's most powerful radio telescope. The GaLactic and Extragalactic All-sky MWA (GLEAM; Wayth et al. 2015) survey observed the whole sky south of declination (Dec) $+30°$ from 2013 to 2015 between 72 and 231 MHz. GLEAM has been processed in a multitude of ways: continuum data releases cover most of the extragalactic sky (GLEAM ExGal; Hurley-Walker et al. 2017), the Magellanic Clouds (For et al. 2018), the Galactic Plane (GLEAM GP; Hurley-Walker et al. 2019b), and a deep region over the South Galactic Pole (GLEAM SGP; Franzen et al. 2021a); and polarisation products include all-sky circular (Lenc et al. 2018) and linear polarisation surveys (Polarised GLEAM Survey (POGS); Riseley et al. 2018; Riseley et al. 2020). Cross-identifications have been provided for the 1863 brightest radio sources in the mid-infrared (the G4Jy Sample White et al. 2020a; White et al. 2020b), and for 1590 galaxies in the 6dF Galaxy Survey (Franzen et al. 2021b).

While GLEAM had lower sensitivity and resolution than other surveys of the time (e.g. the First Alternative Data Release of the Tata Institute for Fundamental Research Giant Metrewave Radio Telescope Sky Survey: TGSS-ADR1; Intema et al. 2017), its major advancement was in leveraging its low frequency and very large fractional bandwidth. Extremely steep spectral indices ($\alpha < -2$, for $S \propto \nu^{\alpha}$) indicate old emission, such as that found in the remnant stage of radio galaxy life cycles (Hurley-Walker
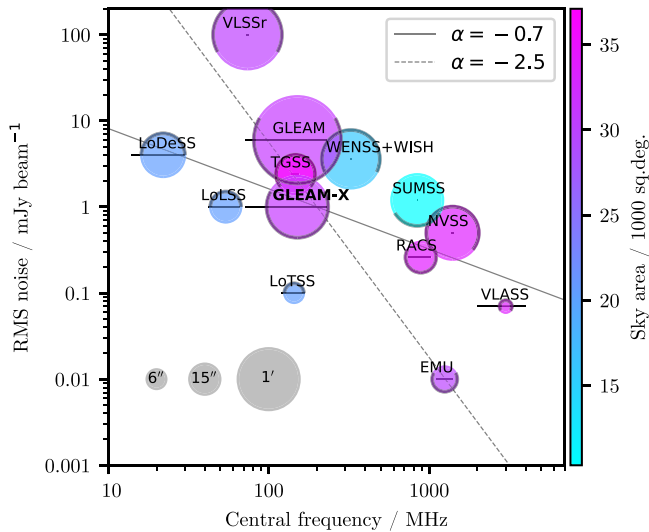
Figure 1. Summary of the sensitivity, frequency, resolution, and sky coverage of a selection of recent and planned large-area radio surveys. The size of the markers is proportional to the survey resolution (full-width-half-maximum of the restoring beam; examples shown in the lower left corner) and their colours show the sky coverage planned. The darkened edges of each marker show the Declination coverage of each survey. The width of each horizontal line shows the frequency range covered by that survey. Representative solid ($\alpha = -0.7$) and dashed ($\alpha = -2.5$) lines show the expected brightness at different frequencies for sources of brightness 1 mJy beam^{-1} at 200 MHz.

et al. 2015; Duchesne & Johnston-Hollitt 2019) or 'fossil' emission in galaxy clusters (Giacintucci et al. 2020); rising spectral indices point toward thermal emission such as found in planetary nebulae (Hurley-Walker et al. 2019b). In this frequency range, absorption effects become important for many sources, allowing measurements to probe synchrotron and free-free absorption in extragalactic radio sources (Callingham et al. 2017) and in Galactic H II regions (Su et al. 2017). Additionally, GLEAM's very high sensitivity to large angular scales, often resolved out by interferometric surveys, enabled exploration of diffuse emission such as Galactic supernova remnants (e.g. Hurley-Walker et al. 2019c) and in clusters of galaxies (e.g. Zheng et al. 2018).

In 2017 the MWA underwent an upgrade to 'Phase II', in which an additional 128 tiles were added to the observatory (Wayth et al. 2018). This enabled observing using two different 128-tile configurations: 'compact', comprising many redundant baselines to improve calibration toward statistical detection of the Epoch of Reionisation (Joseph, Trott, & Wayth 2018), and 'extended', an array optimised for imaging (within the constraints of the observatory) with maximum baselines of 5.5 km, approximately doubling the resolution of the telescope. The latter layout considerably reduces the sidelobes of the synthesised beam, allowing a more 'natural' weighting of the visibility data, which thereby improves the sensitivity of the instrument; sidelobe confusion is also reduced. The smaller main lobe of the synthesised beam reduces the classical confusion limit from ~2 to ~0.3 mJy at 200 MHz (Franzen et al. 2019). These improvements make it more feasible to integrate for longer times and thereby reach lower noise levels without quickly approaching a confusion floor.

While GLEAM enabled a huge range of science outcomes, better modelling of the foregrounds for searches for the Epoch of Reonisation, and flux density scale calibration of the low-frequency southern sky, it is fundamentally limited by its low

(~2′) resolution and the sensitivity limits of the original configuration of the MWA. We therefore undertook a wide-area survey with the Phase II extended array to create GLEAM-X, a deeper, higher-resolution successor to GLEAM, with the same sky and frequency coverage, observed over 2018–2020. During that time, the Long Baseline Epoch of Reionisation Survey (LoBES; Lynch et al. 2021) has demonstrated the survey capability of Phase II by measuring the spectral behaviour of 80824 sources over 100–230 MHz in 3069 deg^2, down to a noise limit of ~2 mJy beam^{-1}, showing the utility of wide-area surveys with the extended array. New radio southern-sky surveys across 800–1400 MHz using the Australian SKA Pathfinder (ASKAP; Hotan et al. 2021) such as the Rapid ASKAP Continuum survey (RACS; McConnell et al. 2020; Hale et al. 2021) have also been developed, offering improved morphological information for millions of radio sources.

Figure 1 shows that the sensitivity of GLEAM-X to ordinary radio galaxies ($-0.8 \lesssim \alpha \lesssim -0.5$) is competitive with other ongoing wide-area surveys such as RACS and the Very Large Array Sky Survey at 3 GHz (VLASS; Lacy et al. 2020). Note also that its sensitivity to steep-spectrum sources ($\alpha = -2.5$) is the same as the upcoming Evolutionary Map of the Universe, which will approach the confusion brightness limit at its frequency (EMU; Norris et al. 2011; 2021). Covering the northern sky at 6–60″ resolution, the LOw-Frequency ARray (LOFAR; van Haarlem et al. 2013) is observing several ongoing surveys: the LOFAR Two-metre Sky Survey (LoTSS; Shimwell et al. 2017), the LOFAR Low-Band Array Sky Survey (LoLSS; de Gasperin et al. 2021), and the LOFAR Decametre Sky Survey (LoDeSS; van Weeren et al., in preparation).

To reach noise levels that are a significant improvement over GLEAM while still covering a wide area, we accumulate a large (~2 PB) volume of visibility data. Releasing processed data products in stages will be of more use to the community than a single data release in the future. This paper is therefore the first in a series of data releases. We release here a pilot survey area that indicates the qualities that can eventually be expected over the full survey, covering 1447 deg^2 over 4 h ≤ RA ≤ 13 h, $-32.7° ≤$ Dec $≤ -20.7°$. Polarisation processing and an associated early data release will be described in a companion paper, Zhang et al. (in preparation). Herein we describe the GLEAM-X observations (Section 2), processing pipeline to produce images and mosaics (Section 3), source-finding to generate catalogues (Section 4), and motivate several extensions to the pipeline (Section 5). Section 6 concludes with an outlook on scientific advances enabled by the survey, and plans for further data releases.

All positions given in this paper are in J2000 equatorial coordinates.

2. Observations

GLEAM used a drift scan survey strategy to quickly and efficiently observe the entire sky south of Dec +30° using the Phase I '128T' configuration of the MWA (Wayth et al. 2015). In the first year (2013 August–2014 June) observations were made along the meridian (HA = 0 h), using seven pointings at Declinations centred on $-72°$ to 18.6°. In the second year, further observations at HA = ±1 h were taken. By combining the GLEAM data in the image plane over the full range of HA for a region around the South Galactic Pole, Franzen et al. (2021a) were able to reach a noise level of 5 mJy beam^{-1} at 215 MHz, about half that of the

extragalactic data release by Hurley-Walker et al. (2017), showing that such a strategy was effective.

GLEAM-X therefore adopted a similar strategy, iterating through the same Declination and HAs as GLEAM, but doubling the number of HA = 0 h observations, and using the extended configuration of the Phase II MWA. Observations were performed in month-long blocks in order to observe similar ranges in RA across the different Declination and HAs, making it easier to combine many drift scans in large mosaics in simple sky projections, improving the uniformity of sensitivity across the sky.

To cover 72–231 MHz using the 30.72-MHz instantaneous bandwidth of the MWA, five frequency ranges of 72–103 MHz, 103–134 MHz, 139–170 MHz, 170–200 MHz, and 200–231 MHz were cycled through sequentially, changing every two minutes. Gain calibrators were visited on an hourly basis in order to provide a back-up in case of unsuccessful in-field calibration (Section 3.1).

After the first observing run in the 2018-A observing semester,[a] the data were triaged to search for poor ionospheric conditions that would hinder high-quality imaging. We determined calibration solutions for the gain calibrator observations on 30-s cadences, and examined the temporal variability between the first and last time-steps for each observation. Seventeen nights were identified as having unacceptably variable gains, with an average of more than 12° of phase change between the first and last time-steps of at least one calibrator, a level at which the imaging quality became very poor. These nights were re-observed in the 2019-A semester. In 2020, the COVID-19 pandemic reduced the observing time available in the 2020-A and B semesters in the extended configuration, so at the time of writing, no further observations to replace any other ionospherically disturbed nights have been possible, although further observations have been proposed for 2022. Table A.1 summarises the observations taken over the period 2018–2020, including those nights that were re-observed.

3. Continuum pipeline

The GLEAM-X pipeline is available on GitHub[b] in a containerised version that can be run on any platform with Singularity installed (Kurtzer, Sochat, & Bauer 2017).

Some common software packages are used throughout the data reduction. Unless otherwise specified:

- To convert radio interferometric visibilities into images, we use the widefield imager WSClean (Offringa et al. 2014) version 2.9, which correctly handles the non-trivial w-terms of MWA snapshot images; versions 2 onward include some useful features such as automatically thresholded CLEANing, and multi-scale CLEAN (Offringa & Smirnov 2017);
- the primary beam is as defined by Sokolowski et al. (2017); however, for speed, all primary beams are precalculated and then interpolated as required using code which is available on github[c] and archived on Zenodo (Morgan & Galvin 2021);
- to mosaic together resulting images, we use the mosaicking software SWARP (Bertin et al. 2002); to minimise flux density loss from resampling, images are oversampled by a factor of four

when being regridded, before being downsampled back to their original resolution;

- to perform source-finding, we use AEGEAN v2.2.5[d] (Hancock et al. 2012; Hancock, Trott, & Hurley-Walker 2018) and its companion tools such as the Background and Noise Estimator (BANE); this package has been optimised for the wide-field images of the MWA, and includes the 'priorised' fitting technique, which is necessary to obtain flux density measurements for sources over a wide bandwidth. Fitting errors calculated by AEGEAN take into account the correlated image noise, and are derived from the fit covariance matrix, which quantifies the quality of fitting; if the fit is poor, and the residuals are large, the fitting errors on position, shape, flux density etc all increase appropriately, so it produces useful error estimates for further use.

We now discuss the typical steps undertaken by the pipeline to produce a set of continuum images and catalogues.

3.1. Calibration

Calibration is performed separately on each observation in a direction-independent manner. The sky model is mainly derived from GLEAM, with additional measurements from the literature for the brighter and more complex sources (e.g. Virgo A in this release). The sky model is described in a companion paper (Hurley-Walker et al. in prep). MITCHCAL (Offringa et al. 2016) is used to generate a calibration solution for each observation, using the full time range of two minutes. These calibration solutions consist of a complex gain for all 4 polarisation products (i.e. a Jones matrix) per tile, per (40-kHz) spectral channel. Since the sky model is limited by the resolution of GLEAM, we exclude baselines longer than the maximum baseline of the 128T configuration, i.e., 2.5 km (1667λ at 200 MHz); to avoid contamination from diffuse Galactic emission, we also exclude baselines shorter than 112 m (75λ at 200 MHz). Calibration solutions are inspected for each night, and tiles or receivers are flagged if they show instrumental issues (e.g. phases appear random with respect to frequency). This typically affects between 1 and 8 of 128 available tiles per night. We also examine whether the solutions are stable within an observation: rapidly changing gains indicate that ionospheric conditions will dramatically reduce imaging quality (as in Section 2). Observations in this category are triaged and do not proceed to imaging (Section 3.7). Similarly, the stability of the gains over the night is inspected; in good conditions, the phases of the solutions only change slowly, on the order of 10° on timescales of hours. If more than 20% of the solutions for a given observation are flagged, we transfer solutions from a well-calibrated observation at the same frequency that is closest in time.

3.1.1. Removing contamination from sidelobe sources

The very brightest radio sources in the sky, the so-called 'A-team' sources (Table 2 in Hurley-Walker et al. 2017), can cause significant image artefacts if they are just outside the field-of-view or in a sidelobe of the primary beam. Additionally, if they are located inside the field-of-view, the standard deconvolution process (Section 3.2) is not always optimal. To remove these sources from the affected observations, we perform a (u,v) subtraction method. The visibilities are phase-rotated to the location of the

source, and a $20' \times 20'$ image of the region is formed, using the following WSCLEAN settings:

- imaging the XX and YY instrumental polarisation products;
- each polarisation product is imaged across 64 480-kHz wide channels that are jointly CLEANed using the `-join-channels` option, which also produces a 30.72-MHz wide multi-frequency synthesis (MFS) for each polarisation;
- a fourth-order polynomial via the `-fit-spectral-pol` argument to constrain the spectral behaviour of each clean component;
- automatic thresholding down to 3σ, where σ is measured as the root mean square (RMS) of the residual XX and YY MFS images at the end of each major cycle;
- a major clean cycle gain of 0.85, i.e. removes 85% of the flux density of the clean components at the end of each major cycle;
- 'Briggs' (Briggs 1995) robust parameter of -1;
- 10 or fewer major clean cycles, in which the images are inverse Fourier transformed back to visibilities, which are subtracted from the data;
- Up to 10^5 minor cleaning cycles, where the subtraction takes place in the image plane.

During this process the 'MODEL' column of the measurement set[e] is updated with the source components, and after it has completed, is subtracted from the calibrated visibilities. The observation is then phase-rotated back to its original location. In this way, the chromatic effect of the primary beam sidelobe is taken into account when removing the source, without distorting the overall gains of the observation.[f]

3.1.2. Polarisation calibration

We also introduce two extra steps in the calibration stage to make the measurement sets ready for polarisation analysis. One is the parallactic angle correction within the primary beam model (Hales 2017), transforming the data from the observed frame (linear feeds on the ground) to an astronomical reference frame according to the IAU standard (polarisation angle measured from North through East). This step is necessary for linear polarisation analysis when observations cover a large range of hour angles. To facilitate later polarisation analysis, we set the cross-terms of the calibration Jones matrices to zero, as well as dividing the Jones matrices for all tiles through by a phasor representing the phases of a reference antenna, which is used for all survey processing. At the same time, we add an X-Y phase determined from observations of a strong polarised source with a known polarisation angle (Lenc et al. 2017). The X-Y phase correction reduces the leakage between linear and circular polarisation, making circularly polarised data available. A detailed description of polarisation calibration, imaging, and a first data release will be given in a separate

publication describing the POlarised GLEAM-X survey (POGS-X; Zhang et al., in preparation).

3.2. Imaging

At this stage, the processing diverges depending on whether there is significant Galactic emission. For this paper, we focus on producing catalogues and images which best explore the extragalactic sky (i.e. without attempting to reconstruct such diffuse emission).

While the original GLEAM survey used an image weighting with a 'Briggs' robust parameter -1, such a weighting is not suitable for the MWA Phase II extended configuration, as the latter has fewer short baselines, reducing the surface brightness sensitivity. For GLEAM-X, a weighting closer to natural is generally preferred to maximise sensitivity (see Hodgson et al. 2020, for a demonstration of the surface brightness sensitivity of MWA Phase II in comparison to other instruments).

To determine an appropriate weighting for extended MWA Phase II imaging, taking into account both angular resolution and surface brightness sensitivity, we trial a range of image weightings, including 'Briggs' weighting with robust parameters 0.0, +0.5, and +1.0, as well as uniform and natural weightings. We simulate simple 2-dimensional Gaussian sources with varying full-width-at-half-maximum (FWHM) in individual template 154-MHz 2-min snapshots after subtracting astronomical sources and noise. Two runs of normal snapshot imaging are performed for each Gaussian source—one with multi-scale CLEAN enabled and the other without. The flux density of the resultant Gaussian sources was then measured using the source-finding software AEGEAN to model the Gaussian component. For the purpose of simulating and measuring the model sources at 3, 5, 10, 20, and 1000σ, and an RMS noise level σ is estimated from real template images for the given image weightings.

Figure 2 shows the various image weightings for the imaging with/without multi-scale CLEAN with the AEGEAN flux density measurements of the sources. A significant increase in the recovered flux density during multi-scale CLEAN motivates its use. The 'best' case for flux density recovery is a natural weighting with multi-scale CLEAN, however with natural weighting the improvement in angular resolution compared to GLEAM is only a factor of ~1.5 and the point source sensitivity is not maximised. To balance an increase in resolution while retaining overall sensitivity, a 'Briggs' robust parameter of +0.5 is chosen for the full survey. We note that the fraction of flux density loss decreases with increasing source brightness. For instance, comparing the top and leftmost two panels of Figure 2, 90% of the flux density is recovered for a $10'$-FWHM 20-σ source, whereas all of the flux density would be recovered for a 1000-σ source of the same size.

While these simulations provide an estimate of the flux density recovery for extended Gaussian sources in snapshot observations, the results shown in Figure 2 should not be used to directly correct flux density measurements made in the final mosaics.

WSCLEAN is used to generate images with the following settings:

- A SIN projection centred on the minimum-w pointing, i.e. hour angle = 0, Dec $-26.7°$
- four 7.68-MHz channels jointly cleaned using the `-join-channels` option, which also produces a 30.72-MHz MFS image;

---

[e]Measurement sets are a common form of data structure for radio interferometric data. They typically consist of three columns: the 'DATA', usually produced directly by the instrument; 'CALIBRATED_DATA' to which some calibration has been applied; and 'MODEL', the model sky sampled by the instrument, which is typically produced either during calibration or imaging.

[f]This differs from the peeling approach used by Hurley-Walker et al. (2017) to process the GLEAM data, which was found to require too much manual intervention for a survey of the size of GLEAM-X.
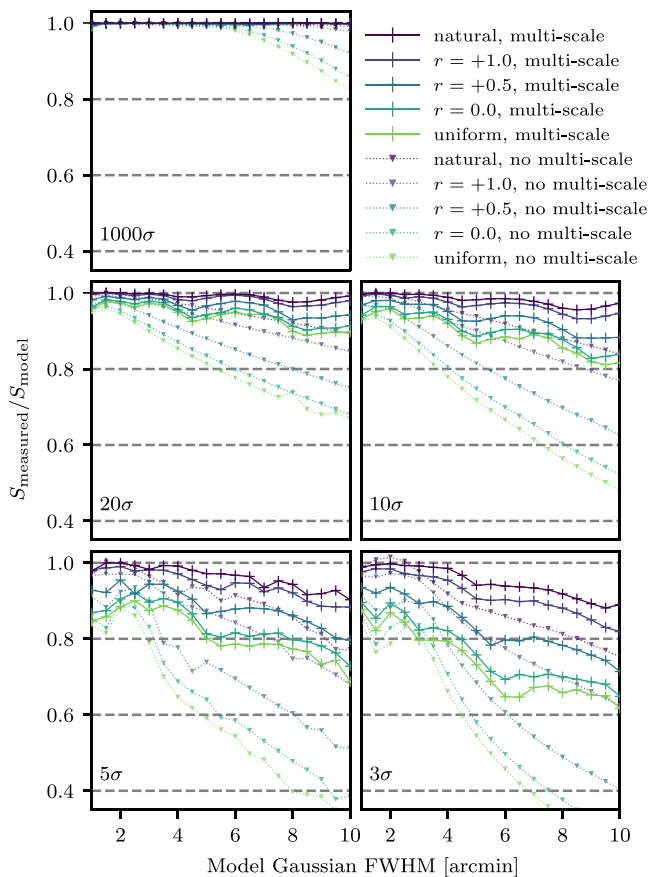
Figure 2. Flux density recovery fraction for model 3, 5, 10, 20, and 1000σ 2-d Gaussian sources with varying FWHM for a range of image weightings. The FWHM range from 60 arcsec up to 600 arcsec in 30 arcsec intervals. The PSF major axis FWHM varies from 80 arcsec (for uniform weighting) to 115 arcsec (for natural weighting). Note the step-pattern visible in the multi-scale cases likely arises due to choice of scales during multi-scale CLEAN.

- include and apply the MWA primary beam (Sokolowski et al. 2017) during cleaning, to produce a Stokes I image;
- automatic thresholding down to 3σ, where σ is the RMS of the residual MFS image at the end of each major cycle;
- automatic CLEANing down to 1σ within pixels identified as containing flux density in previous cycles ('masked' CLEANing);
- a major cycle gain of 0.85, i.e. 85% of the flux density of the clean components are subtracted in each major cycle;
- five or fewer major cycles, in order to prevent the occasional failure to converge during cleaning between 3 and 4σ;
- 10^6 minor cycles, a limit which is never reached;
- multi-scale CLEAN, with the default deconvolution scale settings, and a multi-scale-gain parameter of 0.15;
- 8000 × 8000 pixel images, which encompasses the field-of-view down to 10% of the primary beam;
- 'robust' weighting of 0.5 (see above);
- a frequency-dependent pixel scale such that each image always has 3.5–5 pixels per FWHM of the restoring beam;
- a restoring beam of a 2-D Gaussian fit to the central part of the dirty beam, which is similar in shape (within 10%) for each frequency band of the entire survey, but varies in size depending on the frequency of the observation.

The extended configuration of the Phase II MWA has low sensitivity to sources with extents >10′, and thus is not optimal for recovering the complex emission present in the Galactic Plane. However, the original GLEAM survey was recorded in an identical set of drift scan pointings to GLEAM-X, and at that time the array configuration provided many baselines with sensitivity to these larger angular scales. Thus, for the Galactic plane, we will jointly deconvolve the short baselines of GLEAM with the full GLEAM-X measurement sets, a process enabled by the fast GPU-based image-domain gridding extension to WSCLEAN (van der Tol, Veenboer, & Offringa 2018). This method has been used to great effect to image Fornax A (Line et al. 2020) and Centaurus A (McKinley et al. 2022), and can also be used for other extended sources such as the Magellanic Clouds. An example of these results is shown in Figure 3 and the full description of the process in the context of the Galactic Plane will be demonstrated in a further paper (Hurley-Walker et al., in preparation).

3.3. Astrometric calibration

The ionosphere introduces a λ^2-dependent position shift to the observed radio sources, which varies with position on the sky. Following the method of Hurley-Walker et al. (2017) and Hurley-Walker et al. (2019b), we use FITS_WARP (Hurley-Walker & Hancock 2018) to calculate a model of position shifts based on the difference in positions between the sources in the snapshot and those in a reference catalogue, and then use this model to de-distort the images.

For the reference catalogue, we benefit from using catalogues with similar resolution ($\sim$1′) covering wide areas. For declinations north of −30°, we use NVSS at 1.4 GHz, and for the southern-sky SUMSS at 843 MHz. From this combined catalogue we select a subset which is sparse (no internal matches within 3′) and unresolved (integrated to peak flux density ratio of <1.2).

For each of the 7.68-MHz sub-bands and the wideband 30.72-MHz images formed from each observation, we estimate the background and RMS noise σ using BANE, and perform source-finding using AEGEAN, with a minimum 'seed' threshold of 5σ. Using the iterative catalogue cross-matching functionality of FITS_WARP, we cross-match the measured sources to the reference catalogue, typically finding 1000–3000 cross-matches, from which we retain the 750 brightest sources. A greater number of sources does not improve the accuracy of the warping for typical ionospheric conditions, but does add computational load, so this value was chosen as a point of diminishing returns. These sources typically have flux densities >1 Jy in the NVSS and SUMSS surveys so have adequate astrometry to form the baselines for our corrections.

Snapshot images with fewer than 100 successful cross-matches are discarded (typically <1% of images). The position shifts in the remaining images are typically of order 25″–5″ over 72–231 MHz, and are coherent on scales of 1–20°, similar to previous studies with the MWA (e.g. Hurley-Walker & Hancock 2018; Helmboldt & Hurley-Walker 2020). FITS_WARP uses these position shifts to create a warp model, apply it to all pixels, and interpolate the results back on to the original pixel grid. This technique yields residual astrometric offsets (with no obvious preferred direction or structure) of order 6″ at the lowest frequencies, and 2″ at the highest frequencies.
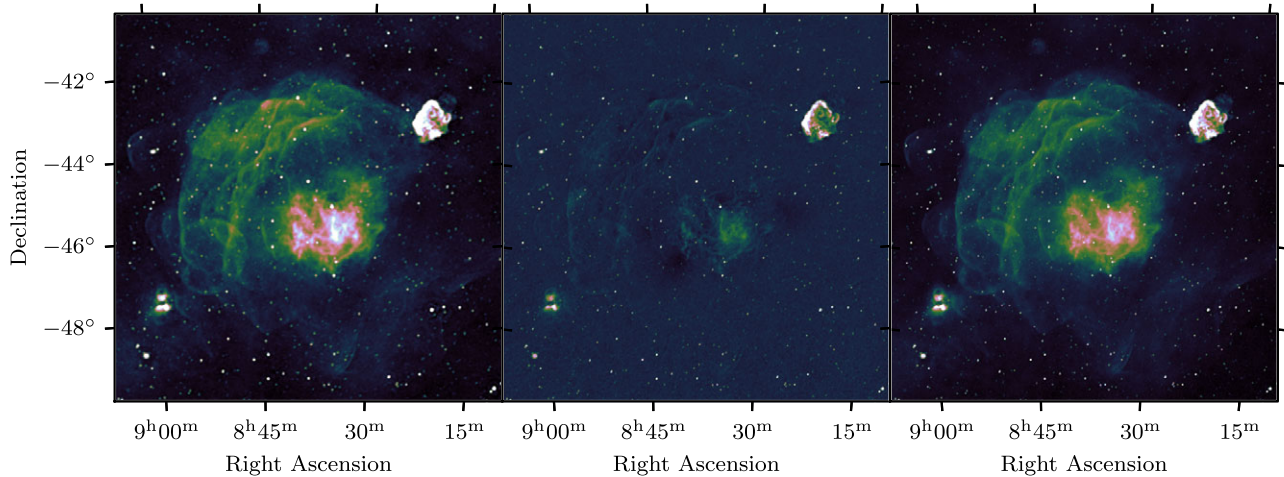
Figure 3. 90 sq. deg. around the Vela supernova remnant at 139–170 MHz. The left panel shows a GLEAM mosaic at 2′.6 resolution; the middle panel shows a GLEAM-X mosaic at 1′.3 resolution; the right panel shows a joint deconvolution of the two datasets yielding the same high resolution, and also the sensitivity to structures on 10′–5° scales.

3.4. Primary beam correction

While the primary beam model developed by Sokolowski et al. (2017) is significantly more accurate than previous models of the MWA primary beam, there remain some discrepancies between our measured source flux densities and those predicted from existing work. In part, this is due to the flagging of individual dipoles in different tiles across the array, which gives these tiles a different and unmodelled primary beam response. For the observations processed in this work, 72 tiles were fully functional, 39 tiles contained one dead dipole, 14 contained two dead dipoles, and three tiles were flagged for having three or more non-functional dipoles. Including the effect of the flagging by computing and using multiple primary beams at the calibration and imaging stages is computationally expensive, so instead a correction is made after the images are formed.

We cross-match each snapshot with a sparse (no internal matches within 5′), unresolved (major axis $a\times$ minor axis $b < 2' \times 2'$) version of the GLEAM-derived catalogue used for calibration (Section 3.1) and make a global mean flux density scale correction using the FLUX_WARP[g] package (Duchesne et al. 2020), typically of order 5–15%. After this global shift, we accumulate the cross-matched tables. Since the discrepancy is consistent in Hour Angle and Dec between snapshots, we can combine the information in this frame of reference.

For each frequency, as a function of HA and Dec, we compare the $\log_{10}$ of the ratio R of the integrated flux densities of the measured source values and reference catalogue. Similarly to GLEAM ExGal, we find no trends with HA, and up to $\pm 10\%$ trends in Dec. Figure 4 shows this effect for a typical frequency band. A fifth-order polynomial model is fitted as a function of Dec using a weighted least-squares fit, where the weights are the signal-to-noise of the sources as measured in each snapshot. The standard deviation of the data from the model ($\sigma_{\rm poly}$) is measured, and sources with $|R| > 3 \times \sigma_{\rm poly}$ are removed from the data. A final model of the same form is fitted to the remaining data, forming a correction function which is then applied to every individual snapshot.
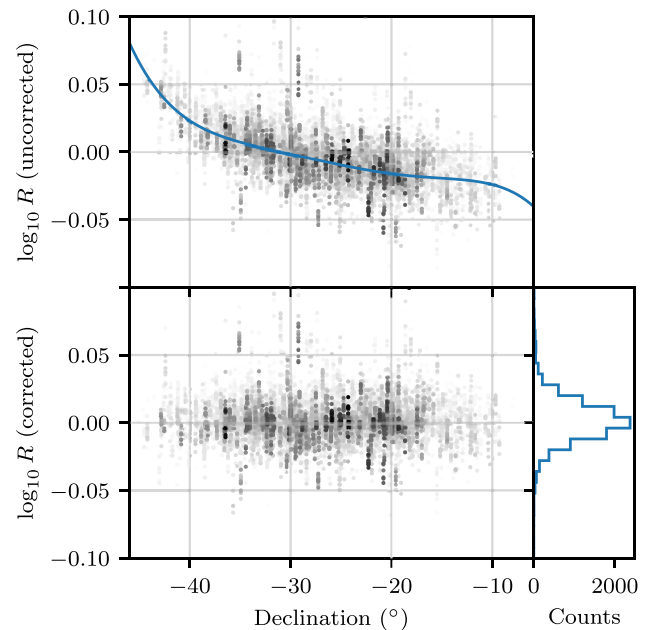
Figure 4. The accumulated flux density scale distribution across the snapshot images at 147–155 MHz from observations performed on 2018 February 20. The upper panel shows the change in $\log_{10} R$ as a function of Dec, where R is the ratio of measured integrated flux density to model integrated flux density. The lower panel shows the same after the polynomial correction function (blue line) has been fit and applied. The adjacent histogram shows the resulting distribution of $\log_{10} R$ over the drift scan. The full-width-at-half-maximum of the resulting histogram is ~2.5%. Similar results are obtained for other frequency bands.

After correction, the primary-beam-corrected 30-MHz MFS images have snapshot RMS values of 35–4 mJy beam^{-1} over 72–231 MHz at their centres, where the primary beam sensitivity is highest.

3.5. Mosaicking

The goal of continuum mosaicking is to combine the astrometrically and primary-beam-corrected snapshot images into deeper images with reduced noise, revealing fainter sources and diffuse

structures invisible in the individual snapshots. For optimal signal-to-noise when mosaicking the night-long scans together, we use inverse-variance weighting. The weight maps are derived from the square of primary beam model, scaled by the inverse of the square of the RMS of the centre of the image, as calculated by BANE.

As discussed in Section 2, GLEAM-X was observed at three different hour angles. This gives each drift scan slightly different (u,v)-coverage, which results in a slightly different restoring beam and thus point spread function (PSF). While each individual drift scan would have a unique and very nearly Gaussian PSF, it could be expected that a stacking of different unique Gaussians with different position angles would result in a non-Gaussian shape. Since most source-finders expect sources to be well-approximated by Gaussians, we tested this effect in our mosaicking procedure. We selected the scans with the most dissimilar (u,v)-coverage where there would be significant overlap in sources, those at HAs -1 and $+1$ from the Dec$+2$ scans, i.e. where the sky is rotating most quickly and projection effects are most important. We simulated a grid of 1 Jy point sources at common RA and Decs for seven observations from each of these scans, and ran them through our imaging and mosaicking stages, using unity image weighting and neglecting unnecessary astrometric and primary beam corrections. We used AEGEAN to source-find on the resulting mosaic, making corrections as necessary for the projection (Section 4). We recovered the sources at integrated flux densities of 0.995–0.999 Jy and peak flux densities of 0.96–0.97 Jy beam^{-1}. Subtracting these Gaussian fits from the image plane data, we found residuals at the $<4.5\%$ level, indicating that level of deviation away from Gaussianity. Since the integrated flux densities were recovered well, and the non-Gaussianity is fairly small, even for this worst-case scenario, we adopt this mosaicking method going forward.

For each 7.68-MHz frequency channel, we form a night-long drift scan, and examine it to check for any remaining data quality issues. We also form five 30.72-MHz bandwidth mosaics from the multi-frequency synthesis images generated during cleaning (Section 3.2). After quality checking, for each frequency, data from all four nights that cover the same RA range are combined together to make a single deep mosaic. At this stage, we also form a 60-MHz bandwidth 'wideband' image over 170–231 MHz, as this gives a good compromise between sensitivity and resolution, and will be used for source-finding (Section 4).

3.6. Calculation of the PSF

As described in Appendix A of Duchesne et al. (2020), imaging away from the phase centre incurs a significant phase rotation during re-gridding as part of the mosaicking process. This re-projection results in a point-spread function that is not defined at the image reference coordinates. This is corrected partially by introduction of a projected regrid factor, f, that is applied to the PSF major axis to form an 'effective' PSF major axis. For a resultant ZEA projection this is simply related to the change in solid angle over the original SIN-projected image with (e.g. Thompson, Moran, & Swenson 2001)

$$f = \sqrt{1 - l^2 - m^2} \,, \qquad (1)$$

where l and m are the direction cosines defined with reference to the *original*, SIN-projected image direction. The ZEA projection itself reduces additional area-related projection effects due to its equal area nature. This is used in initial source-finding on

the mosaics as the integrated flux density is correct and the product of the major and minor PSF axes is also correct for the new projection.

Residual uncorrected ionospheric distortions can cause slight blurring of the final mosaicked PSF. This can be characterised by examining sources which are known to be unresolved, which is best determined by using a higher-resolution catalogue than our calibration sky model; we thus use the NVSS and SUMSS combined catalogue described in Section 3.3. Following Hurley-Walker et al. (2017, 2019b), we cross-match this catalogue with the sources detected in our mosaics at signal-to-noise >10, and then measure the size and shape of these sources in the GLEAM-X mosaics. We create a PSF map by averaging and interpolating over these sources, using Healpix (order$= 4$, i.e. pixels $\sim 3°$ on each side) as a natural frame in which to accumulate and average source measurements.

After the PSF map has been measured, its antecedent mosaic is multiplied by a (position-dependent) 'blur' factor of

$$B = \frac{a_{\mathrm{PSF}} b_{\mathrm{PSF}}}{a_{\mathrm{rst}} b_{\mathrm{rst}}} \qquad (2)$$

where a_{rst} and b_{rst} are the FWHM of the major and minor axes of the restoring beam, and a_{PSF} and b_{PSF} are the FWHM of the major and minor axes of the PSF. This has the effect of normalising the flux density scale such that both peak and integrated flux densities agree, as long as the correct, position-dependent PSF is used (Hancock et al. 2018). Values of B are typically 1.0–1.2.

3.7. Final images

The mosaicking stage of Section 3.5 results in 26 mosaics: one with 60-MHz bandwidth, five with 30-MHz bandwidth and the other 20 covering 72–231 MHz in 7.68-MHz narrow bands. In this work, we run the pipeline on four nights of observing indicated in Table A.1, producing a large set of mosaics with decreasing sensitivity toward the edges. Here we downselect to a region which is representative of the survey's eventual sensitivity, covering $4\,\mathrm{h} \leq \mathrm{RA} \leq 13\,\mathrm{h}$, $-32.7° \leq \mathrm{Dec} \leq -20.7°$, for further analysis. Figures 5–7 show this area for four of the deeper mosaics. Postage stamps of these images are available on both SkyView and the GLEAM-X website.[h] The header of every postage stamp contains the PSF information calculated in Section 3.6, and the completeness information calculated in Section 4.3.

We use BANE to determine the background and RMS noise of each mosaic. During development of this survey, we noticed that BANE's default of three loops of 3-sigma-clipping is insufficient to exclude source-filled pixels to accurately determine the background and RMS noise. The issue may not have been noticed in previous works due to the relatively higher sensitivity and resulting source density of GLEAM-X (although Hurley-Walker et al. (2017) noted a similar effect from the high sidelobe confusion levels of GLEAM). We modified BANE to use 10 loops and found that it produced more accurate noise and background estimates (see Section 4.2.2 for further analysis). Figure 8 shows an example of 10 sq. deg of the 170–231 MHz wideband mosaic and associated background and RMS noise, as well as the same region as seen by GLEAM ExGal, in which the resolution is lower, the noise is higher, and the diffuse Galactic synchrotron on scales of $>1°$ is visible.

---

[h]https://www.mwatelescope.org/gleam-x.
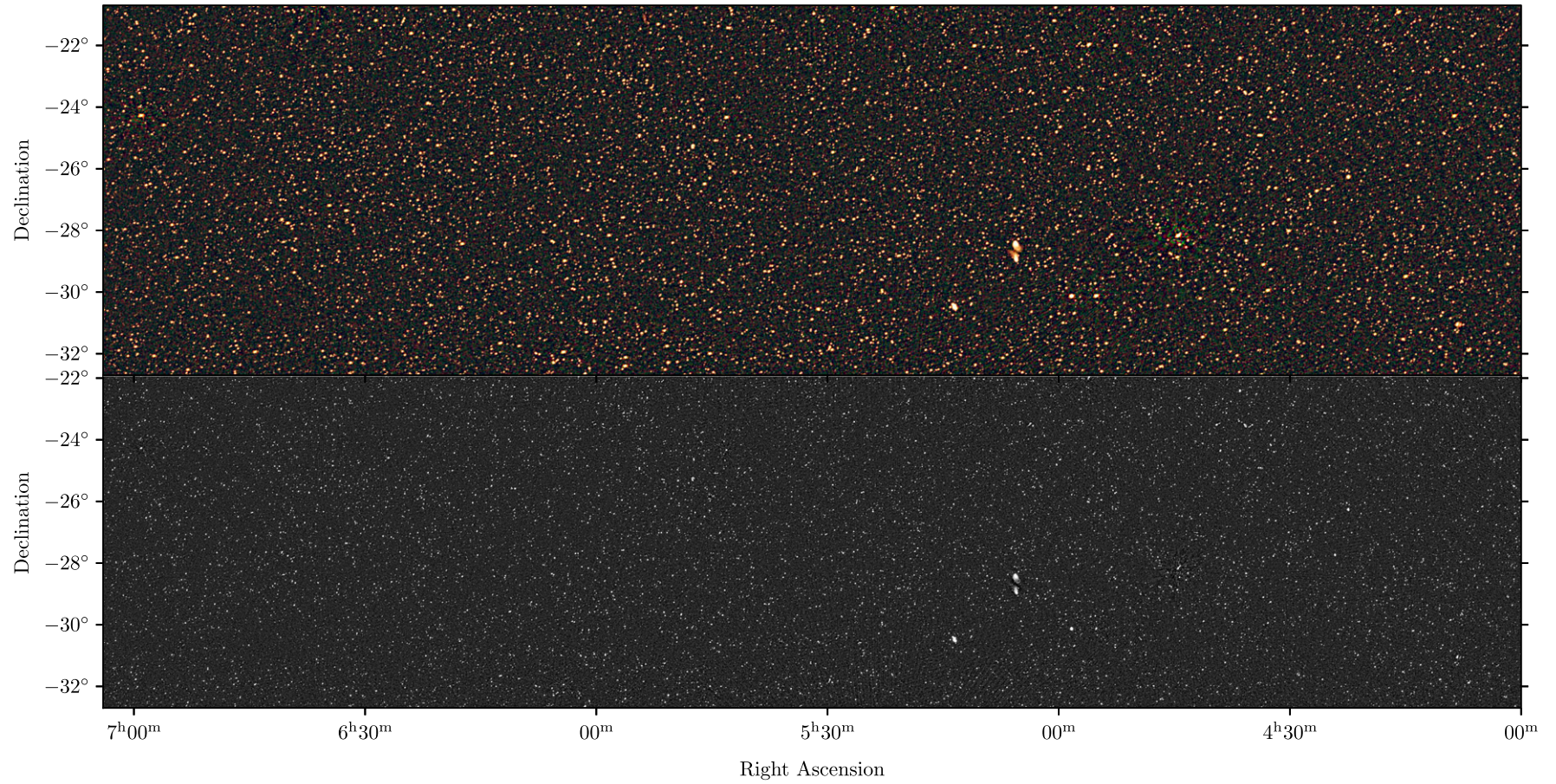
Figure 5. Continuum mosaics from this data release, for RA 4–7 h. In each sub-panel, the top image shows the 72–103 MHz (R), 103–134 MHz (G), and 139–170 MHz (B) data as an RGB cube, with an arcsinh stretch spanning −9–200 mJy beam^{-1}; the lower image shows the 170–231 MHz source-finding image, with an arcsinh stretch spanning −3–200 mJy beam^{-1}.

Figure 6. Continuum mosaics from this data release, for RA 7–10 h. Figure formatting is identical to Figure 5.

Figure 7. Continuum mosaics from this data release, for RA 10–13 h. Figure formatting is identical to Figure 5.

Figure 8. Ten sq. deg. of the wideband source-finding mosaic centred on RA 10^h30^m Dec$-27°30'$; the left panel shows the image from GLEAM ExGal; the middle panel shows the image from this work; the top and bottom right panels show, respectively, the background and RMS noise of the GLEAM-X data as measured by 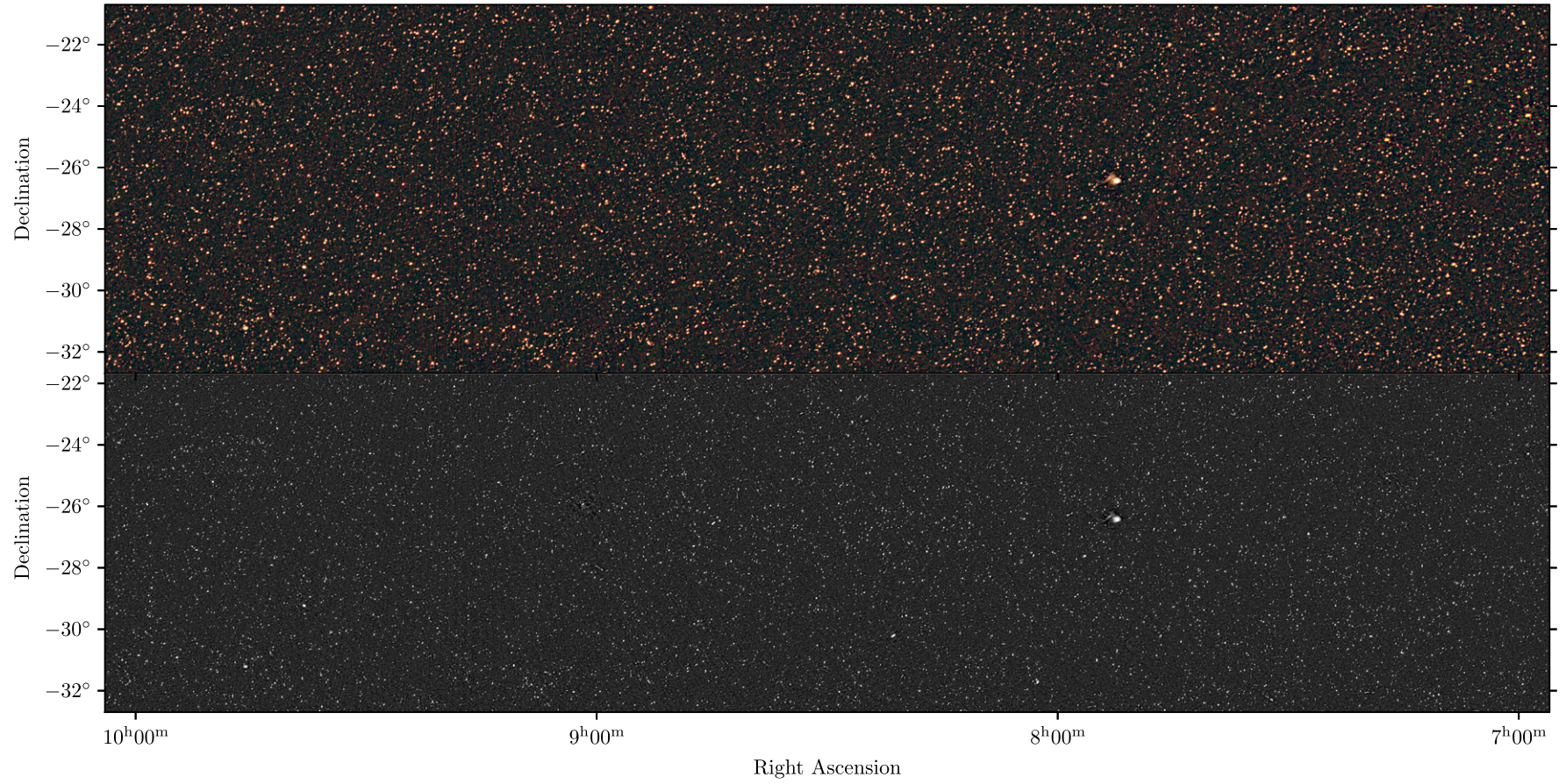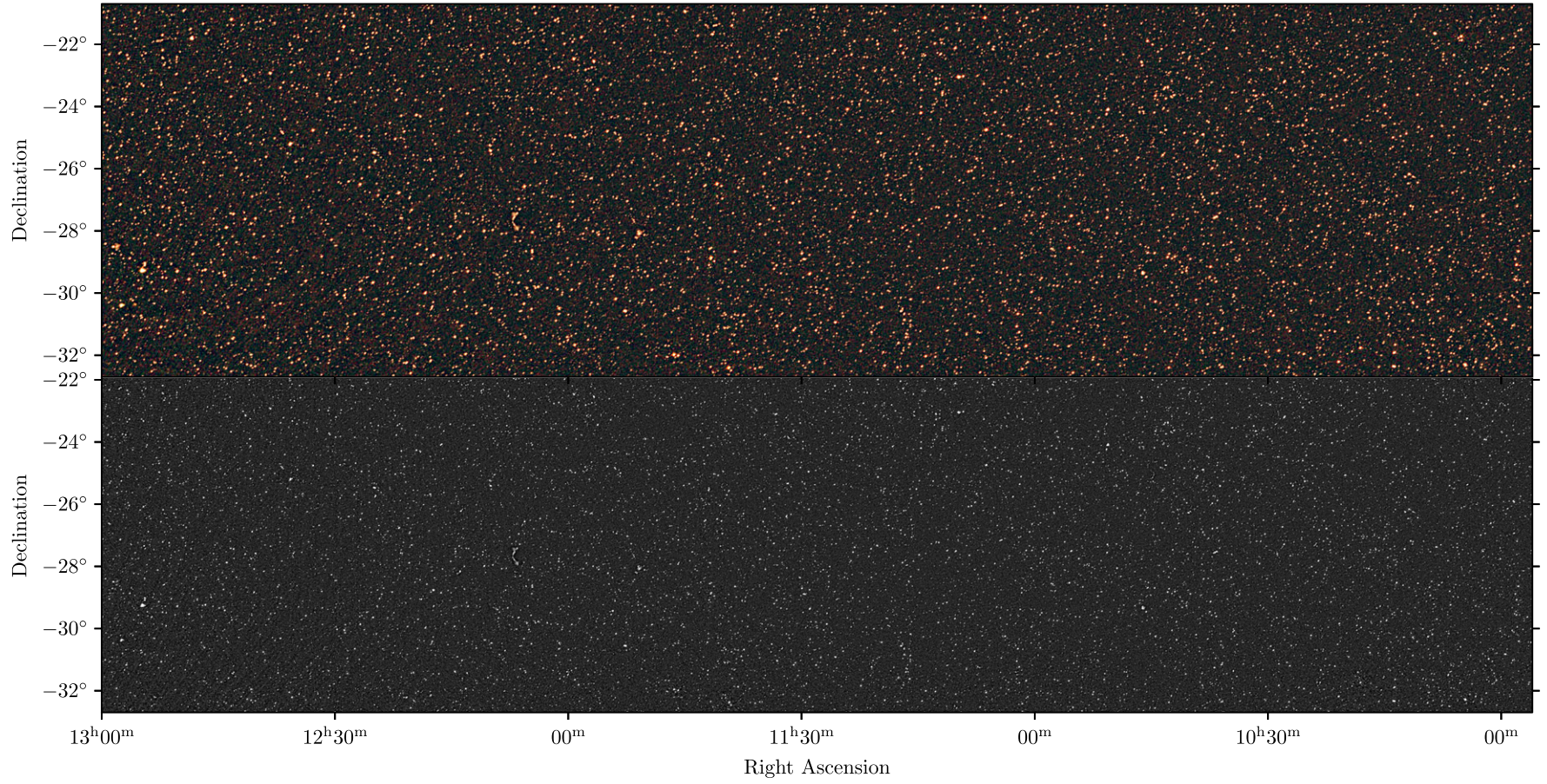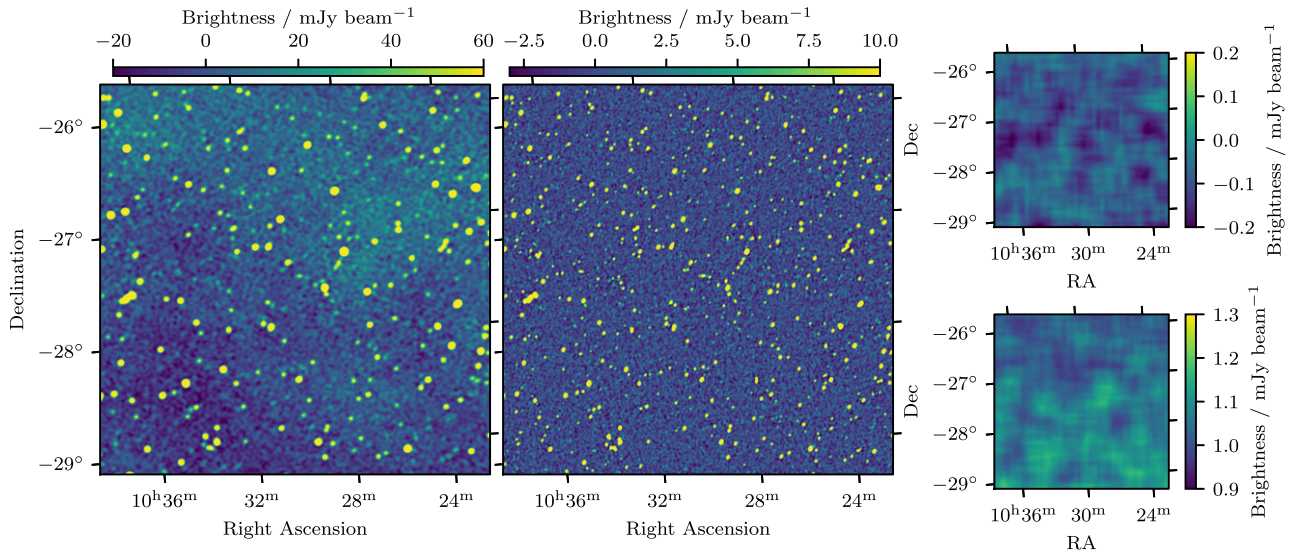BANE. GLEAM ExGal contains 212 components in this region, and the average RMS noise is 6 mJy beam^{-1}; GLEAM-X contains 548 components and the average RMS noise is 1.1 mJy beam^{-1}.

Combining data in the image plane may lead to the recovery of faint sources that were not cleaned during imaging. The RMS noise levels in the wideband (30-MHz) mosaics range from 5–1.3 mJy beam^{-1} over 72–231 MHz. This compares to typical snapshot RMS values of 35–4 mJy beam^{-1} over the same frequency range (Section 3.4). Cleaning is performed down to 1-σ for components detected at 3-σ in a snapshot (Section 3.2). The centres of each image form the greatest contribution to each mosaic due to weighting by the square of the primary beam (Section 3.5). We can therefore estimate at what signal-to-noise threshold uncleaned sources will typically appear: $\frac{3\times35}{5} = 21$ – $\frac{3\times4}{1.3} = 9$ from 72–231 MHz, and at $\sim\frac{3\times4}{1} = 12$ in the wideband (60-MHz) source-finding image (Section 4).

Modelling this effect, especially in conjunction with Eddington bias (see e.g. Section 4.2.1), which is also significant at these faint flux densities, lies beyond the scope of this paper. It would involve significant work and is mainly of interest for performing careful measurement of low-frequency source counts (see Franzen et al. 2019, for an equivalent analysis for GLEAM). At this stage we merely suggest additional caution when using flux densities for sources at low (<12) signal-to-noise.

The mosaics at this stage are only a subset of the GLEAM-X sky. The RMS increases toward the edges due to the drop in primary beam sensitivity and selected RA range of these observations. Future mosaics comprised of further nights of observing will be combined to produce near-uniform sensitivity across the sky.

4. Compact source catalogue

A source catalogue derived from the images is a useful data product that enables straightforward cross-matching, spectral fitting, and population studies. We aim here to accurately capture components of sizes $<10'$ across all frequency bands, fitting elliptical two-dimensional Gaussians with AEGEAN. We carry out this process on the $1447-\deg^2$ region selected in Section 3.5, and the steps are generally applicable to future mosaics produced from the survey.

4.1. Source detection

We follow the same strategy as Hurley-Walker et al. (2017): using the 170–231 MHz image, a deep wideband catalogue centred at 200 MHz is formed. We set the 'seed' clip to four, i.e. pixels with flux density $>4\sigma$ are used as initial positions on which to fit components, where σ denotes the local RMS noise. After the sources are detected, we filter to retain only sources with integrated flux densities $\geq 5\sigma$. We then use the 'priorised' fitting technique to measure the flux densities of each source in the narrow-band images: the positions are fixed to those of the wideband source-finding image, the shapes are predicted by convolving the shape in the source-finding image with the local PSF, and the flux density is allowed to vary. Where the sources are too faint to be fit, a forced measurement is carried out. We perform several checks on the quality of the catalogue, detailed below.

4.2. Error derivation

In this Section we examine the errors reported in the catalogue. First, we examine the systematic flux density errors; then, we examine the noise properties of the wideband source-finding image, as this must be close to Gaussian in order for sources to be accurately characterised, and for estimates of the reliability to be made, which we do in Section 4.3. Finally, we make an assessment of the catalogue's astrometric accuracy. These statistics are given in Table 1.

4.2.1. Comparison with GLEAM

GLEAM forms the basis of the flux density calibration in this work, and in this Section we examine any differences between the flux densities measured here compared to those measured by GLEAM ExGal. We select compact sources from both catalogues (integrated/peak flux density <2) that cross-match within a $15''$ radius, and have a good power law spectral index fit (reduced $\chi^2 \leq 1.93$; see Section 4.4). Curved- and peaked-spectrum sources comprise only a small proportion of the catalogue and are more likely to be

Table 1. Survey properties and statistics, for the region published in this paper, in comparison to the largest single data release from GLEAM (Hurley-Walker et al. 2017), and estimates for the full survey. Values are given as the mean, ± the standard deviation where appropriate. The statistics shown are derived from the wideband (170–231 MHz) image. The internal flux density scale error applies to all frequencies.

Property	GLEAM-X (this release)	GLEAM ExGal	GLEAM-X (full)
Number of sources	78967	307456	1.7 M
Number of sources spectrally fit	71320	254453	1.5 M
Sky area	1, 447 deg^2	24402 deg^2	30954 deg^2
Source density	55 deg^{-2}	13 deg^{-2}	55 deg^{-2}
RA astrometric offset	$+14 \pm 700$ mas	$-4 \pm 16''$	$\sim 20 \pm 700$ mas
Dec astrometric offset	$+21 \pm 687$ mas	$0.1 \pm 3.6''$	$\sim 20 \pm 700$ mas
Internal flux density scale error	2%	2%	2%
50% completeness	5.6 mJy	55 mJy	5.6 mJy
90% completeness	10 mJy	170 mJy	10 mJy
98% completeness	50 mJy	500 mJy	50 mJy
Reliability for $S_{int} \geq 7\sigma$	99.7%	99.8%	99.7%
Reliability for $S_{int} \geq 5\sigma$	98.2%	98.9%	98.2%
Image RMS noise	1.27 ± 0.15 mJy beam^{-1}	11.3 ± 7.3 mJy beam^{-1}	~ 1.2 mJy beam^{-1}
PSF major axis	$77 \pm 12''$	$152 \pm 25''$	~ 75–$110''$
PSF minor axis	$61 \pm 6''$	$134 \pm 12''$	$\sim 60''$

variable (Ross et al. 2021), so are not included in this check. We excluded all sources in GLEAM-X data which have a cross-match within 2′ in order to avoid selecting sources which are unresolved in GLEAM and resolve into multiple components in GLEAM-X.

As surveys approach their detection limit, measured source flux densities are increasingly likely to be biased high due to noise; there are a larger number of faint sources available to be biased brighter by noise than there are bright sources available to be biased dimmer. Eddington (1913) describes corrections that can be made to an ensemble of measurements to remove this bias. For the purpose of this section, we wish to correct the individual GLEAM flux density measurements in order to check the GLEAM-X flux density scale. We use Equation (4) of Hogg & Turner (1998) to predict the maximum likelihood true flux density of each of the GLEAM 200-MHz measurements:

$$S_{corrected} = \frac{S}{2} \left(1 + \sqrt{\frac{4q + 4}{\frac{S^2}{\sigma}}} \right) \tag{3}$$

where σ is the local RMS noise, and q is the logarithmic source count slope (i.e. the index in $\frac{dN}{dS} \propto S^q$); at these flux density levels $q = 1.54$ (Franzen et al. 2016).

Figure 9 plots the ratio of the two catalogue integrated flux densities as a function of signal-to-noise in GLEAM-X, with a correction applied to the GLEAM flux densities. The ratio trends toward 1.05 at higher flux densities, although the very brightest sources show only small discrepancies from unity. Since the effect is small, we do not attempt to correct for it here, but may revisit our data processing in future to see if it can be reduced, corrected, or eliminated. Since the flux density scale is tied to GLEAM, which has an 8% error relative to other surveys, this value may be used as an error when combining the data with other work.

No obvious trends are visible in the fitted spectral indices (Figure 10); we note that the error bars on the GLEAM-X measurements are uniformly smaller due to the increased signal-to-noise of the data.
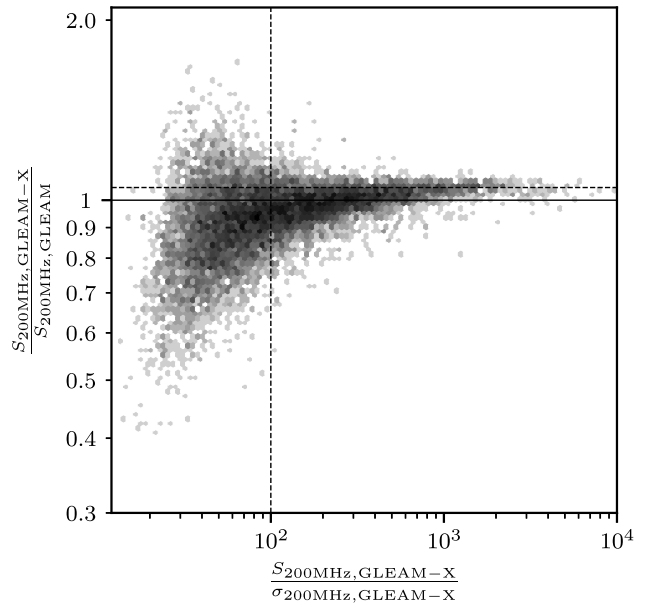
Figure 9. The ratio of the 200-MHz integrated flux densities measured in GLEAM-X and GLEAM, as a function of signal-to-noise in GLEAM-X, for compact sources matched between the two surveys in the region released in this work. The horizontal black line shows a ratio of 1 and the horizontal dashed black line shows a ratio of 1.05, which is a better visual fit at high signal-to-noise. The vertical line is plotted at a signal-to-noise of 100, approximately the 90% completeness level of GLEAM in this region. The error bars are omitted for clarity, but as the quadrature sum of the measurement errors in both surveys, increase to $\sim$10% at the 90% completeness limit of GLEAM, and to $\sim$30% at the faintest levels.

4.2.2. Noise properties

We briefly examine the noise properties of the source-finding 170–231-MHz image. We use a 18 deg^2 region centred on RA 10^h30^m Dec$-27°30'$ with fairly typical source distribution. Following

Figure 10. Spectral indices α from the spectra fitted across the 20 7.68-MHz narrow bands of GLEAM-X (ordinate) against GLEAM (abscissa), for compact sources matched between the two surveys in the region released in this work. The colour axis shows an arbitrary number density scaling to show where there are more points. The error bars are the fitting errors obtained for each source, dominated by the flux density calibration error at the bright end and the local RMS noise at the faint end. The diagonal line shows a 1:1 ratio.
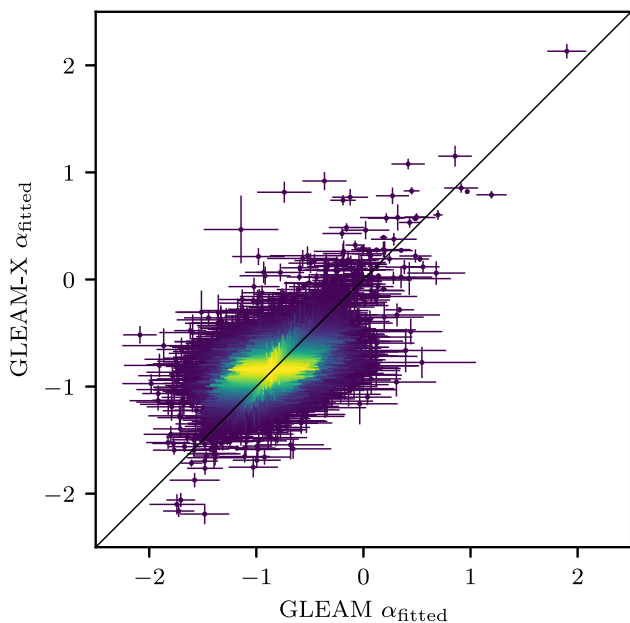
Hurley-Walker et al. (2017), we measure the background of the region using BANE, and subtract it from the image. We then use AᴇRᴇs ("Aᴇɢᴇᴀɴ REsiduals") from the Aᴇɢᴇᴀɴ package to mask out all sources which were detected by Aᴇɢᴇᴀɴ, down to $0.2\times$ the local RMS. We also use AᴇRᴇs to subtract the sources to show the magnitude of the residuals. Histograms of the remaining pixels are shown, for the unmasked and masked images, in Figure 11.

The higher resolution of the GLEAM-X survey compared to GLEAM means that confusion forms a smaller fraction of the noise contribution, and thus the noise distribution is almost completely symmetric. Surveys close to the confusion limit will see a skew toward a more positive distribution, as seen by Hurley-Walker et al. (2017). Noise and background maps are made available as part of the survey data release.

4.2.3. Astrometry

Following Hurley-Walker et al. (2017), we measure the astrometry using the 200-MHz catalogue, as this provides the locations and morphologies of all sources. To determine the astrometry, high signal-to-noise (integrated flux density $>50\sigma$) GLEAM-X sources are cross-matched with the isolated sparse NVSS and SUMSS catalogue (Section 3.3); the positions of sources in these catalogues are assumed to be correct and RA and Dec offsets are measured with respect to those positions. The average RA offset is $+14 \pm 700$ mas, and the average Dec offset is $+21 \pm 687$ mas (errors are 1 standard deviation).

In 99% of cases, fitting errors on the positions are larger than the measured average astrometric offsets. Given the scatter in the measurements, we do not attempt to make a correction for these offsets. As each snapshot has been corrected, residual errors should not vary on scales smaller than the size of the primary beam. Figure 12 shows the density distribution of the astrometric offsets, and histograms of the RA and Dec offsets, which were used to calculate the values listed in this section.

4.3. Completeness and reliability

4.3.1. Completeness

Following the same procedure as Hurley-Walker et al. (2017), simulations are used to quantify the completeness of the source catalogue at 200 MHz, using the wideband mosaics. 26 realisations are used in which 25000 simulated point sources of the same flux density were injected into the 170–231 MHz mosaics (at approximately 20% of the true source density). The flux density of the simulated sources is different for each realisation, spanning the range 10^{-3} to $10^{-0.5}$ Jy in increments of 0.1 dex. The positions of the simulated sources are chosen randomly but not altered between realisations; to avoid introducing an artificial factor of confusion in the simulations, simulated sources are not permitted to lie within $5'$ of each other. Sources are injected into the mosaics using AᴇRᴇs. The major and minor axes of the simulated sources are set to a_{psf} and b_{psf}, respectively.

For each realisation, the source-finding procedures described in Section 4 are applied to the mosaics and the fraction of simulated sources recovered is calculated. In cases where a simulated source is found to lie too close to a real ($>5\sigma$) source to be detected separately, the simulated source is considered to be detected if the recovered source position is closer to the simulated rather than the real source position. This type of completeness simulation therefore accounts for sources that are omitted from the source-finding process through being too close to a brighter source.

Figure 13 shows the fraction of simulated sources recovered as a function of S_{200MHz}. The completeness is estimated to be 50% at $\sim$5.6 mJy rising to 90% at $\sim$10 mJy; these flux densities were typically below the RMS noise in GLEAM ExGal. Errors on the completeness estimate are derived assuming Poisson errors on the number of simulated sources detected. Figure 14 shows the spatial distribution of the completeness for the work presented here; the slight dependence on RA is largely due to the presence of bright sources in large mosaics, e.g. Hydra A at $\sim$RA 09^{h}20^m Dec $-12°$. The roll-off in Declination is due to the primary beam sensitivity of the single drift scan used in this work; in the full survey, multiple drift scans will be used to ensure near-uniform sensitivity and completeness across the sky.

The completeness at any pixel position is given by $C = N_d/N_s$, where N_s is the number of simulated sources in a circle of radius $6°$ centred on the pixel and N_d is the number of simulated sources that were detected above 5σ within this same region of sky. The completeness maps, in FITS format, can be obtained from the supplementary material. Postage stamp images also include the estimated completeness at representative flux densities in their headers.

4.3.2. Reliability

To test the reliability of the source finder and check how many of the detected sources might be false detections, we use the same source-finding procedure as described above but search only for negative peaks. Aᴇɢᴇᴀɴ is run with a seedclip of 4σ (allowing for detections with peaks above this limit) and detections outside of the central region are cut. This initially yields 1144 negative
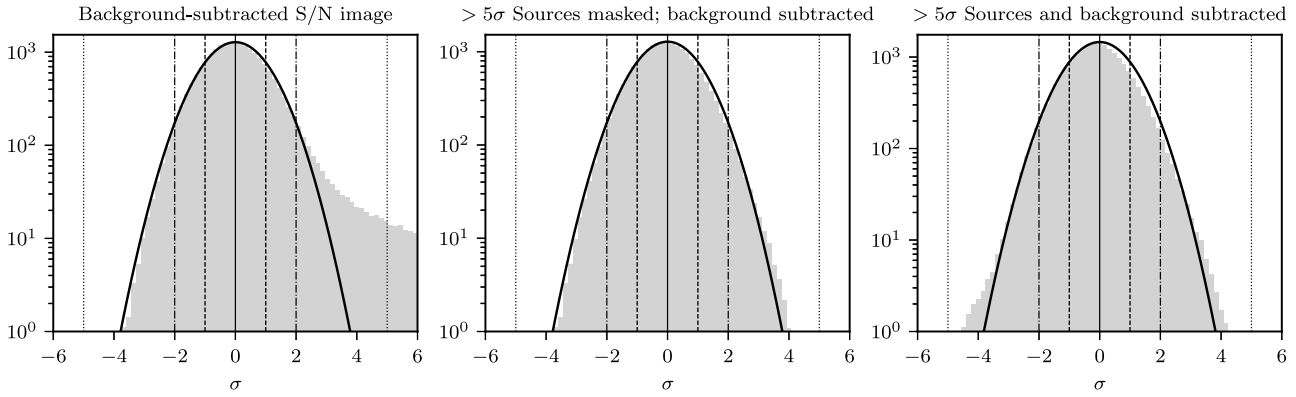
Figure 11. Noise distribution in a typical 18 square degrees of the wideband source-finding image. BANE measures the average RMS in this region to be 1.06 mJy beam^{-1}. To more clearly show any deviation from Gaussian noise, the ordinate is plotted on a log scale. The leftmost panel shows the distribution of the S/Ns of the pixels in the image produced by subtracting the background and dividing by the RMS map measured by BANE; the right panel shows the S/N distribution after masking all sources detected at 5σ down to 0.2σ. The light grey histograms show the data. The black lines show Gaussians with σ = 1; vertical solid lines indicate the mean values. |S/N| = 1σ is shown with dashed lines, |S/N| = 2σ is shown with dash-dotted lines, and |S/N| = 5σ is shown with dotted lines.
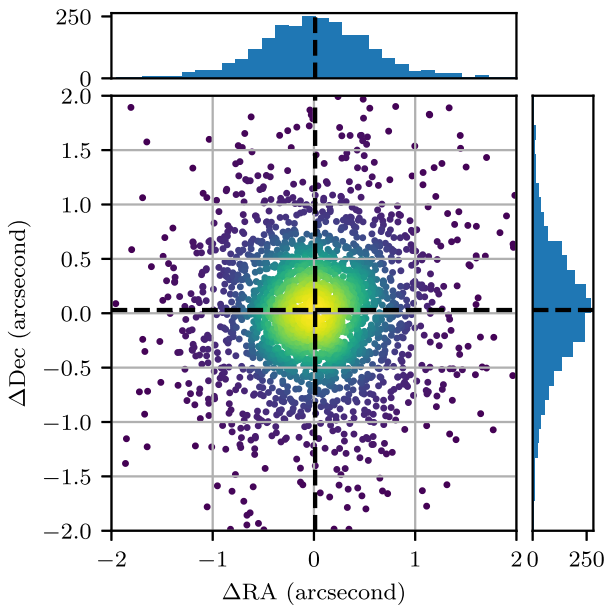
Figure 12. The astrometric offsets of 19771 isolated, compact, >50-σ sources after cross-matching against the NVSS and SUMSS reference catalogue described in Section 4.2.3 Vertical and horizontal dashed lines indicate the mean offset values in the RA and Dec directions, respectively. Similarly, the horizontal and vertical histograms 0highlight the counts of the astrometry offsets in each direction.

detections. Filtering the results to retain only sources with integrated flux densities $S_{int} > 5\sigma$ leaves 198 detections. Inspection revealed that some of these detections were artefacts around very bright sources, rather than noise peaks (see Figure 15). There were also similar positive detections of artefacts around these bright sources. We filtered out any detections (positive or negative) that were

- within 5′ of a positive detection whose peak flux density was ≥2 Jy and where the absolute value of the ratio of the fainter peak to the bright peak was ≥350; or
- within 12′ of a positive detection whose peak flux density was ≥6 Jy and where the absolute value of the ratio of the fainter peak to the bright peak was ≥650.
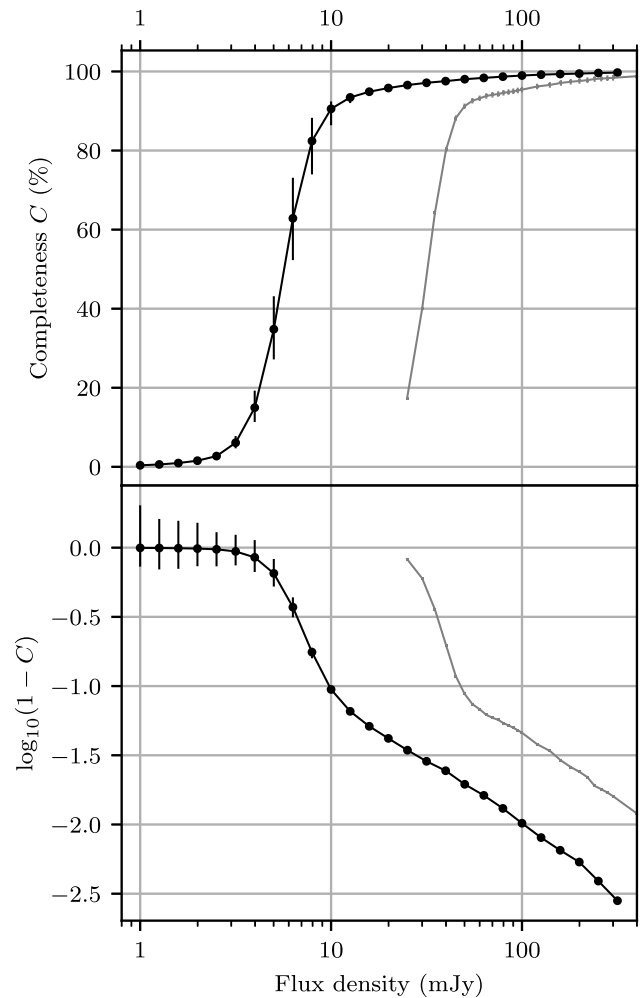
Figure 13. Completeness as a function of integrated flux density at 200 MHz for the region published in this work, which has RMS noise 1.27 ± 0.15 mJy beam^{-1}. The top panel shows the completeness C; to better display the completeness as it approaches 100%, the bottom panel shows $\log_{10}(1 - C)$. Black markers and lines indicate GLEAM-X; for comparison, grey markers and lines show the completeness of GLEAM for a low-noise region used to determine source counts in GLEAM ExGal (∼2500 deg^2 with RMS noise 6.8 ± 1.3 mJy beam^{-1}).
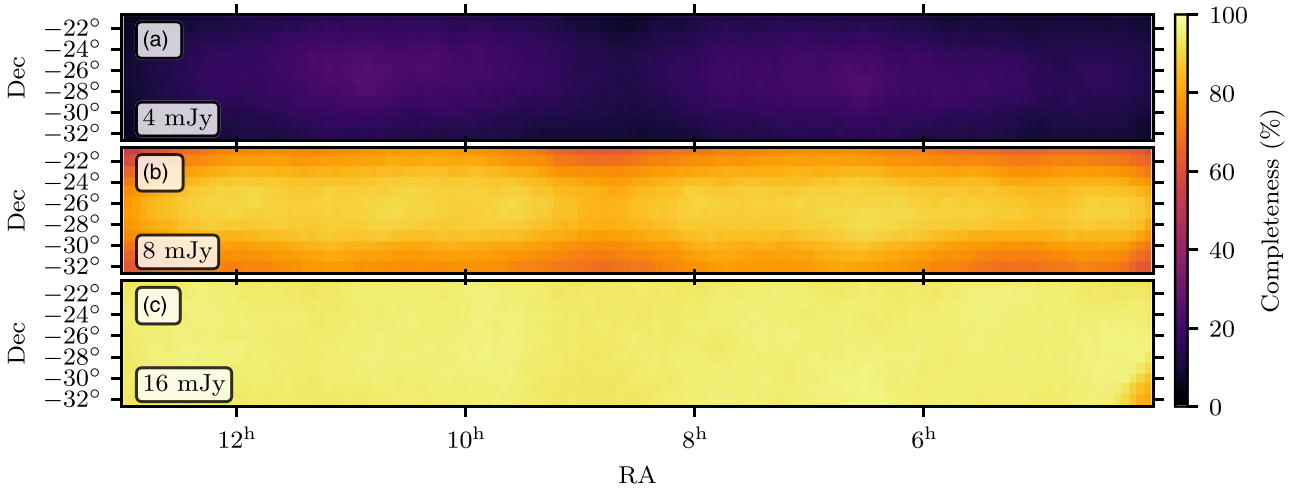
Figure 14. Completeness fraction as a function of position on the sky for three representative cuts in source integrated flux density at 200 MHz, for the catalogue released in this work.
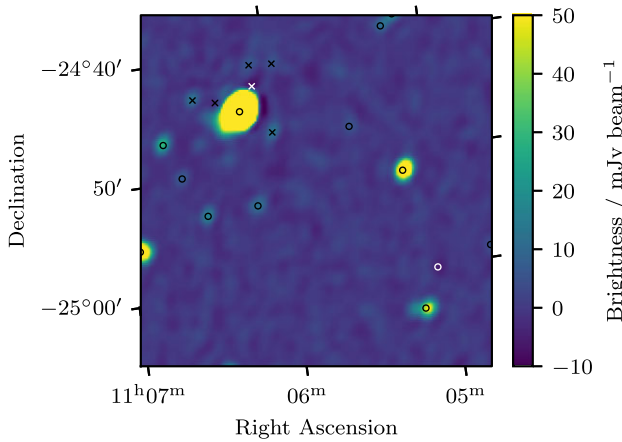
Figure 15. An example of filtering artefacts that present as spurious positive and negative sources around very bright sources. Black circles indicate detected positive components that are not filtered, while black ×s show positive components that are filtered. The white circle shows a negative source that was not filtered, while the white × shows a negative source that was filtered for being too close to a bright source.

Figure 16. An example of a negative source found next to a positive source that could optionally be filtered when generating the reliability estimate. Black circles indicate detected positive components that are not filtered; the white + shows a negative source that can optionally be filtered.

This accounts for the moderately bright artefacts closer in to the bright sources and fainter artefacts that can exist further out from very bright sources. This filtering cuts 157 positive detections and 149 negative detections.

We also note that there is a tendency for negative sources to appear close to positive sources regardless of their brightness, potentially due to faint uncleaned sidelobes slightly reducing the map brightness very close to sources. These negative sources will not have positive counterparts, so potentially can also be filtered before estimating the reliability. The criterion in this case is that they cross-match with a positive source within 2′. An example is shown in Figure 16. These comprise a further 46 sources which may optionally be removed.

Comparing the filtered samples of negative to positive detections, we can estimate the number of positive detections that are false detections as a function of signal to noise. For a conservative estimate, where we do not apply the second filter, we find that at a signal-to-noise ratio of five, the number of false detections is

just under 2%, falling quickly to 1% for $S_{int} > 5.5\sigma$. If we also filter negative sources that lie close to positive sources, we find that the reliability is much higher, with only 0.75% of sources false at 5-σ, and rising to none at 8-σ. For each significance bin, we convert these fractions to a reliability estimate and plot them as a function of signal-to-noise in Figure 17. We note that were the noise completely Gaussian, we would expect just one +5σ source in this sky area to appear purely by chance, and none with flux density >5.5σ; i.e., a reliability of 99.999% in the faintest bin, rising quickly to 100%.

4.4. Spectral fitting

We fit two models to the twenty narrow-band flux density measurements for all detected sources (using $S \propto \nu^\alpha$). The first model is a simple power law parameterised as

$$S_\nu = S_{\nu_0} \left(\frac{\nu}{\nu_0} \right)^\alpha, \qquad (4)$$
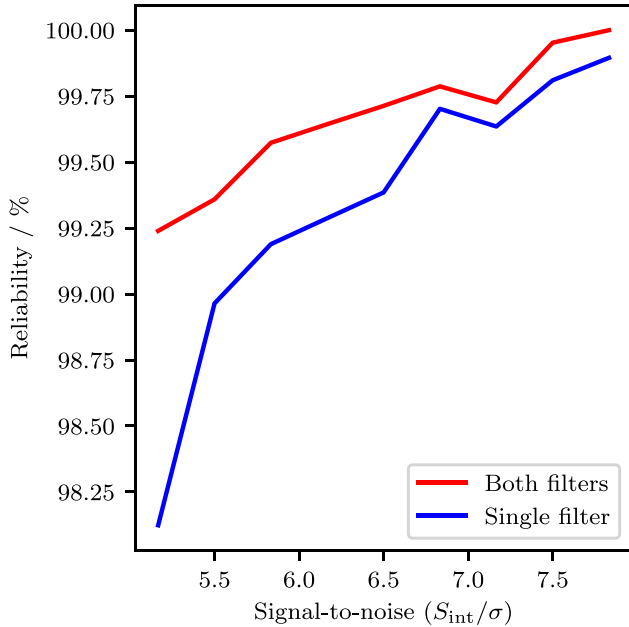
Figure 17. Estimates of the reliability of the catalogue as a function of signal to noise. The lower blue curve shows a conservative estimate without filtering negative sources detected on the edges of positive sources. The upper red curve shows a more generous estimate derived after filtering these sources out. In comparison, GLEAM ExGal has a reliability of 98.9%–99.8% at these signal-to-noise levels.

where S_{ν_0} is the brightness of the source, in Jy, at the reference frequency ν_0, and α describes the gradient of the spectral slope in logarithmic space. We also extend this power law model to,

$$S_\nu = S_{\nu_0} \left(\frac{\nu}{\nu_0}\right)^\alpha \exp\left(q\ln\left(\frac{\nu}{\nu_0}\right)^2\right), \tag{5}$$

which includes the additional free parameter q to capture any higher order spectral curvature features, where increasing $|q|$ captures stronger deviations from a simple power law; if q is positive, the curve is opening upward (convex) and if q is negative, the curve is opening downward (concave). This model is not physically motivated, and may not appropriately describe sources with different power law slopes in the optically thin and thick regimes, but provides a useful filter to identify interesting sources. For both models we set ν_0 to 200-MHz.

To perform accurate spectral fitting, the errors on the flux density measurements must be known. Following Hurley-Walker et al. (2017), spectral fitting allows us to check the flux density consistency of the catalogue. A flux density scaling error of 2% yields a median reduced χ^2 of unity across the catalogue, whereas higher or lower values bias the reduced χ^2 lower or higher as a function of signal-to-noise. We thus adopt 2% as the measure of our internal flux density scale, and set the errors on the flux density to this value added in quadrature with the local fitting error from AEGEAN. (Note that 8% is more appropriate when comparing with other catalogues as this is the flux density scale accuracy of GLEAM, to which GLEAM-X is tied (see Section 4.2.1).)

We applied the Levenberg-Marquardt non-linear least-squares regression algorithm (as implemented in the SCIPY PYTHON module; Virtanen et al. 2020) to Equations (4) and (5) for each detected source. We did not include narrow bands with negative integrated flux density measurements. We discarded the fitting results if

- there were fewer than 15 integrated flux density measurements for a source;
- a χ^2 goodness-of-fit test indicated at a $>99\%$ likelihood of an incorrectly fit model; or
- $q/\Delta q < 3$, to ensure constrained deviations from a power law are statistically significant.

For this initial data release we included only the model with the lower reduced-χ^2 statistic in our catalogue. Applying these criteria a total of 70432 and 888 source components have fitting results recorded for power law and curved power law models, respectively. Figure 18 shows five example SEDs, four with either power law or curved power law models constrained using exclusively GLEAM-X, and one with GLEAM-X data supplemented with data from SUMSS and NVSS to fit a two-component power law model described as

$$S_\nu = \frac{S_p}{1 - \exp(-1)} \times \left(1 - \exp\left(-\left(\frac{\nu}{\nu_p}\right)^{\alpha_{\text{thin}} - \alpha_{\text{thick}}}\right)\right) \left(\frac{\nu}{\nu_p}\right)^{\alpha_{\text{thick}}}$$

where S_p is the brightness (Jy) at the peak frequency ν_p (MHz), and α_{thin} and α_{thick} are the spectral slopes in the optically thin and optically thick regimes, respectively (Callingham et al. 2017).

For sources fit well by power law SEDs, the distributions of spectral indices α with respect to flux density are plotted in Figure 19. The median α for the brightest bin is -0.83, in excellent agreement with previous results (e.g. Mauch et al. 2003; Lane et al. 2014; Heald et al. 2015).

The priorised fitting routine in AEGEAN separates the island finding stage from the component characterisation stage, and is analogous to aperture photometry in optical images (Hancock et al. 2018). We use this in GLEAM-X to ensure that each radio-component identified in our deep 170–231 MHz source-finding image has an equivalent component characterisation in each of the other 25 GLEAM-X images. This process however does not enforce spectral smoothness between images adjacent in frequency. For GLEAM-X, this process becomes less reliable towards lower frequencies, where the PSF becomes large enough that nearby components are blended to the point where their brightness profiles cannot be distinguished. Although model optimisation methods may be able to constrain the total brightness across all components, the brightness between individual components become degenerate. We highlight an example of this behaviour in Figure 20. This problem is most apparent for sources that are slightly resolved and characterised as two separate components within $120''$ from one another. Further development of AEGEAN to perform component characterisation across all images jointly while including physically motivated parametrisation of the spectra is planned to address this issue.

4.5. Final catalogue

The resulting catalogue consists of 78967 radio sources detected over 1447 deg^2. 71320 sources are fit well by power law or curved-spectrum SEDs. The catalogue has 388 columns (see Appendix B) and is available via Vizier. The catalogue measurements can be used to perform more complex spectral fits, especially in conjunction with other radio measurements. Table 1 shows the properties of the images and catalogue in this data release, as well as some forward predictions for the full survey, in comparison to GLEAM.
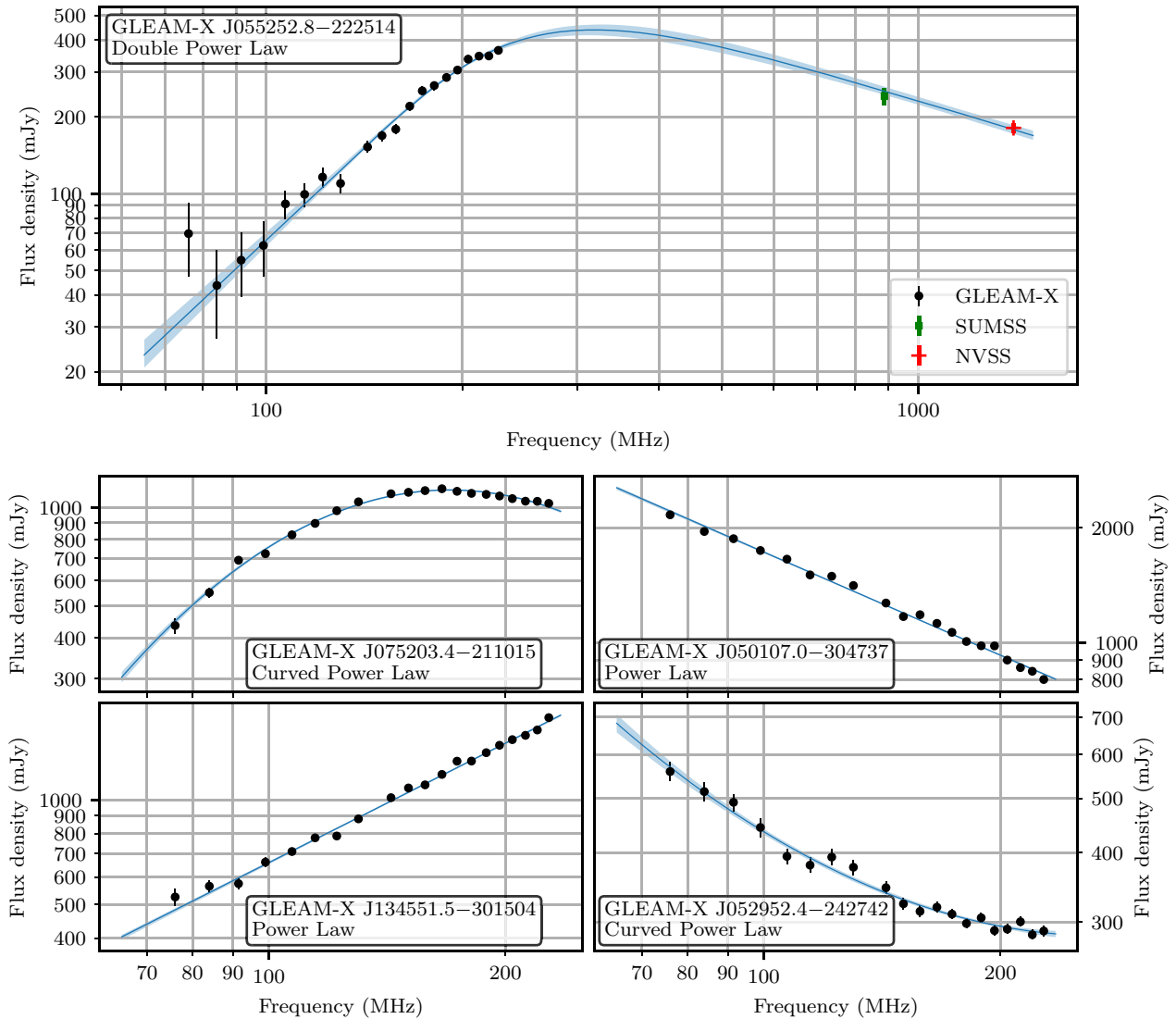
Figure 18. Five example SEDs of sources selected to highlight the variety of spectral shapes seen within the GLEAM-X data. The panel inset includes the source name and model used to fit the presented data. The optimised model and its 1-σ confidence interval is overlaid as the blue line of each source. The 'Power Law' and 'Curved Power Law' are defined as Equations (4) and (5), respectively. The 'Double Power Law' used for GLEAM-X J055252.8−222514 shows Equation (3) of Callingham et al. (2017) fitted using the GLEAM-X data and higher frequency measurements from SUMSS and NVSS.

5. Extensions to continuum processing

The total data volume of GLEAM-X visibilities is large (∼2 PB) and file transfer operations comprise a significant proportion (∼40%) of our processing time. When processing the data, each observation takes up ∼100 GB of disc space in visibilities, images, and metadata. Given the richness of the GLEAM-X survey, we are strongly motivated to perform additional operations on the data while they reside on disc in order to avoid moving the data more frequently. In this section we discuss the current extensions to the pipeline that we expect will yield a range of science outcomes not possible with mosaicked images.

5.1. Transient imaging

The wide field-of-view of the MWA combined with the repeated drift scanning strategy of GLEAM-X yields a dataset that is interesting to search for transient radio sources. Murphy et al.

(2017) compared the first GLEAM catalogue with TGSS-ADR1 and found a single transient candidate, but understanding its nature was difficult with the (limited) data available. Historically this has been a common occurrence for low-frequency radio transients, with many unusual phenomena detected but never fully understood (e.g. Hyman et al. 2005; Stewart et al. 2016; Varghese et al. 2019).

The GLEAM-X drift scans were observed such that the LST was matched for repeated observations at the same pointing and frequency. This enabled a search using 'visibility differencing', wherein calibrated measurement sets were differenced, and the resulting nearly empty visibilities were inverted to form a dirty image, which could be used to search for transient sources (Honours thesis: O'Doherty 2021; Hancock et al. in prep.). One high-significance candidate was followed up using the large MWA archive, resulting in the discovery of a new type of highly polarised radio transient, repeating on the unusual timescale of 18.18 min
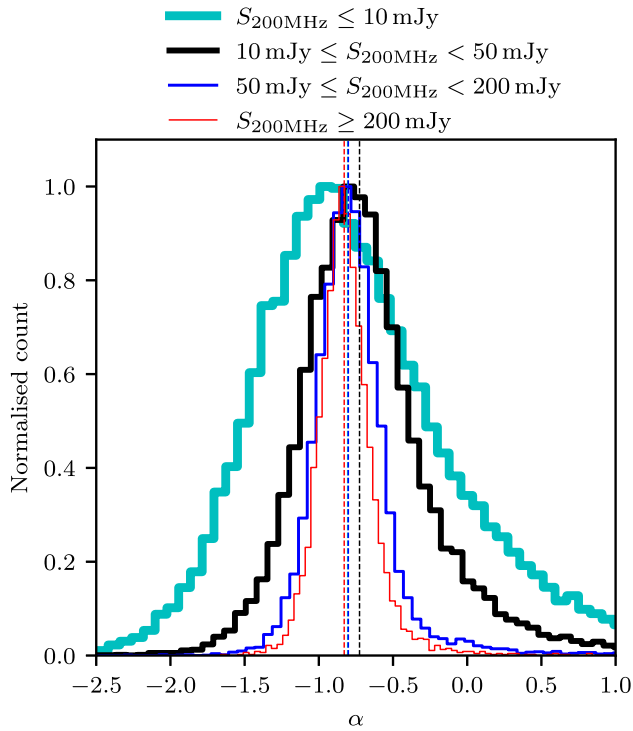
Figure 19. The spectral index distribution calculated for sources where the fit was successful (reduced $\chi^2 < 1.93$). The cyan line shows sources with $S_{200\mathrm{MHz}} < 10$ mJy, the black line shows sources with $10 \leq S_{200\mathrm{MHz}} < 50$ mJy, the blue line shows sources with $50 \leq S_{200\mathrm{MHz}} < 200$ mJy, and the red line shows sources with $S_{200\mathrm{MHz}} > 200$ mJy. The dashed vertical lines of the same colours show the median values for each flux density cut: -0.81, -0.73, -0.80, and -0.83, respectively.

(Hurley-Walker et al. 2022). The wide bandwidth of GLEAM-X was key to finding the dispersion measure of the source, and therefore estimating its distance.

The visibility differencing approach resulted in a large number of false positives due to the differences in ionospheric conditions between observations. The discovery of a new type of radio transient, and the utility of our polarisation and wideband measurements, motivates the inclusion of a transient imaging step in our routine pipeline processing.

Our approach is to image every 4-s interval of each observation, at the same time subtracting the deep model that was formed during imaging (Section 3.7), the same approach that is currently used for imaging MWA interplanetary scintillation observations (Morgan et al., in preparation). This results in a thermal-noise-dominated Stokes I image cube where only differences between each time step and the continuum average are recorded. This cube is then stored in an HDF5 file[i] as described in Appendix 2 of Morgan et al. (2018). Briefly, the image cube is reordered so that time is the fastest axis, and the pixel data is demoted to half precision (16-bit) floats. This results in a typical data volume of 600 MB per observation. Once in this format, any number of algorithms can be conveniently applied to detect and measure time-domain signals.

While imaging every 0.5-s sample would be ideal, it would multiply by 8× the storage and processing requirements for all other

[i]www.hdfgroup.org/HDF5.
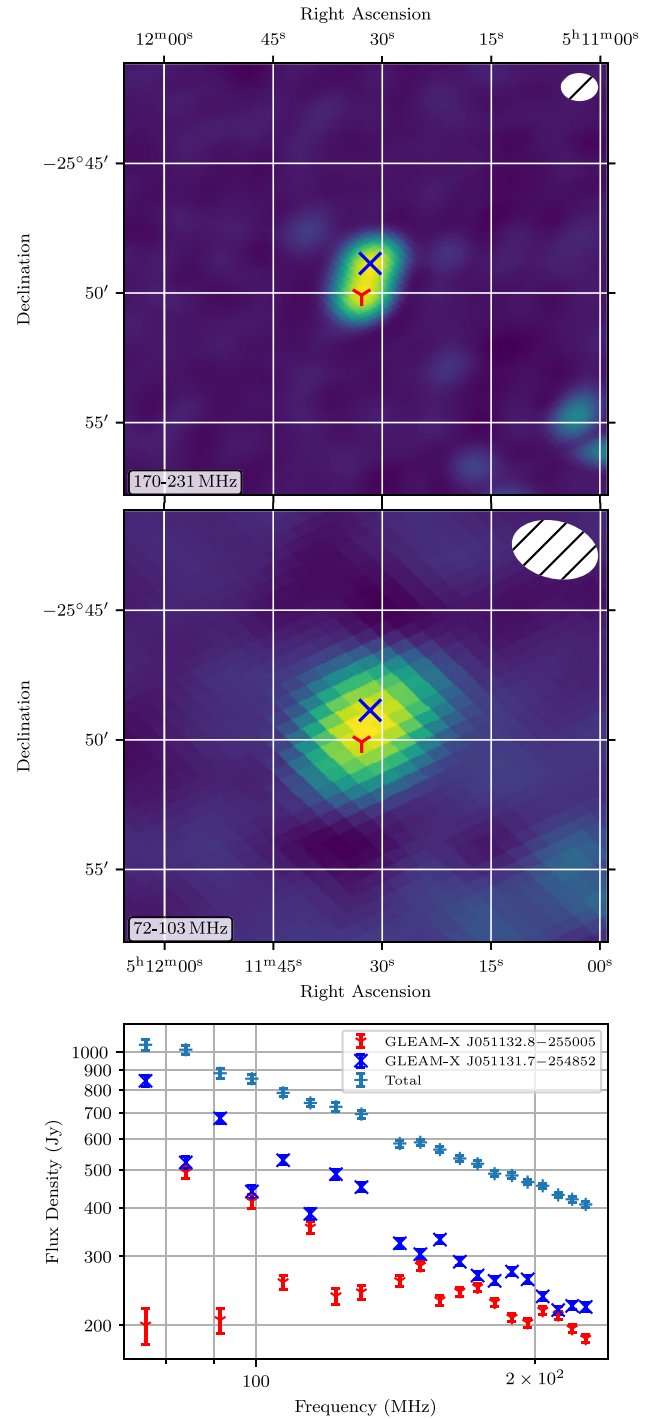
Figure 20. An example where the AEGEAN priorised fitting routine was unable to produce consistent flux density measurements across sub-bands for a pair of components (GLEAM-X J051132.8 − 255005 and GLEAM-X J051131.7 − 254852) belonging to a single island. The top and middle panels are the 170–231 MHz and 72–103 MHz images towards these components, respectively, and the white ellipse in the upper right corner is the corresponding PSF. The bottom panel contains the SEDs of the individual components and their total.

steps of the pipeline, but if a signal of interest is discovered then it is simple (and indeed necessary) to reprocess the data with higher time (and, if needed, frequency) resolution. Future data releases will provide these data and quantitative analyses thereof.
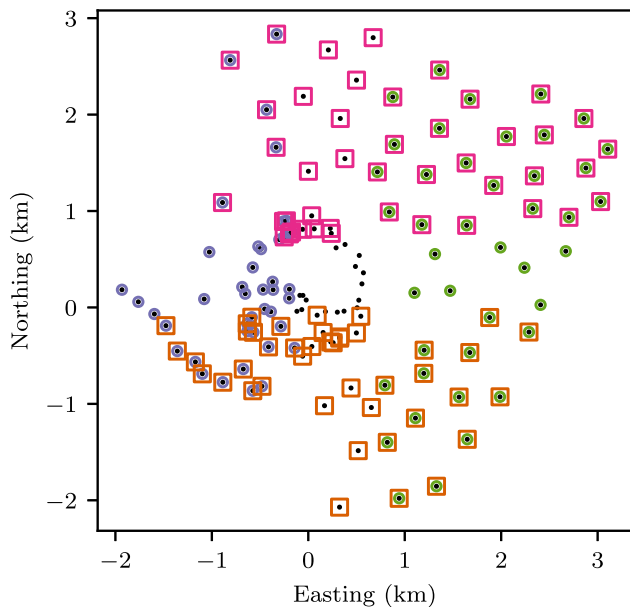
Figure 21. The layout of the tiles comprising the MWA Phase II extended configuration, overlaid with symbols representing sub-arrays used for ionospheric binocular imaging (Section 5.2). Pink and orange squares show the North and South pair, while green and lavender circles indicate the East and West pair.

5.2. Binocular imaging

The source position offsets determined during the de-warping process (Section 3.3) yield information about the slant total electron content (dTEC) averaged over the telescope array projected on to the sky in that field-of-view. If dTEC varies significantly over the array, the wavefronts from different parts of the sky will arrive at different times, and radio sources will appear stretched, duplicated, or will disappear completely. Conversely, if images are created using sub-arrays of the telescope, the apparent difference in source positions can be used to constrain an approximate height of the distorting screen (Loi et al. 2015; Helmboldt & Hurley-Walker 2020). We thus add a module to the imaging pipeline to routinely produce these binocular images.

In choosing the sub-arrays from the extended Phase II, we face a compromise between sensitivity (higher for large sub-arrays) and parallax lever arm (better for widely separated sub-arrays). Additionally we have no prior knowledge of what ionospheric activity will be observed on the night, nor the resources to adjust the imaging to match at the time of processing. To form a generally useful product, we split the array into two pairs of sub-arrays following the cardinal directions, shown in Figure 21. Each group of 43 or 44 antennas is imaged separately, and source-finding is performed using the default settings of AEGEAN. These catalogues can form a useful input to future analyses of the ionosphere above the Murchison Radio-astronomy Observatory; the data and analysis will be released in future work.

6. Outlook and conclusions

In this work we described GLEAM-X, a new wideband low-frequency all-southern-sky survey performed using the MWA, as well as the data reduction steps we expect to use to produce a range of continuum data products over 72–231 MHz. Polarisation data will be described in the upcoming paper by Zhang et al.

(in preparation). Extensions to our data reduction pipeline to perform transient searches (Section 5.1) and binocular imaging (Section 5.2), as well as joint deconvolution of the Galactic Plane (Figure 3) will further enhance the capabilities of the survey.

To demonstrate the quality and attributes of the images and catalogues that will be produced by GLEAM-X, we release here 1447 deg^2 of sky in the form of 26 mosaics across 72–231 MHz of bandwidths 60, 30, and 8 MHz, with RMS noises ranging from 15 to just over 1 mJy beam^{-1}. Additionally, we form a catalogue of 78967 sources, 70432 of which are well-fit across our band with power law spectral energy distributions, and 888 with curved power law spectra. Extrapolating our source density of 55 deg^{-2} to the $\sim$31000 deg^2 that GLEAM-X will eventually cover, we expect to detect of order 1.7 M sources, and produce $\sim$1.5 M radio spectra.

We plan to release the survey in a series of data releases; the next will comprise a large ($\sim$15000 deg^2) set of images and catalogues covering the southern extragalactic sky centred on the South Galactic Pole (Galvin et al., in preparation); secondly we aim to process and release the complete Galactic Plane (Hurley-Walker et al., in preparation); finally, we will aim to produce contiguous all-sky coverage. Polarisation, transient, and ionospheric data releases and analyses will also proceed over coming years.

These data will enable a range of science outcomes, some of which are outlined by Beardsley et al. (2019) in their review of scientific opportunities with Phase II of the MWA. For instance, there is strong potential to detect 10^4 peaked-spectrum sources in GLEAM-X data, an order of magnitude more than discovered by GLEAM (Callingham et al. 2017), and also probing a population an order of magnitude fainter. Improved signal-to-noise on sources with curved and peaked spectra can provide more efficient selection of high-redshift radio galaxies (Drouart et al. 2020). Many local star-forming galaxies will be resolved, enabling better understanding of the interplay between thermal and non-thermal processes in their energy budgets (Kapińska et al. 2017; Galvin et al. 2018).

The extended configuration of the Phase II MWA has already been used very capably for targeted investigations of the extragalactic sky, such as determining the remnant radio galaxy fraction in one of the Galaxy and Mass Assembly fields (Quici et al. 2021) and detecting diffuse non-thermal emission in galaxy clusters (Duchesne, Johnston-Hollitt, & Bartalucci 2021). Similar studies over the whole sky, particularly exploiting synergies with other recent wide-area surveys such as RACS, are likely to be highly productive. The higher source density of GLEAM-X will for the first time enable cosmological measurements with the MWA. We can resolve the tension between the angular clustering observed with NVSS and TGSS-ADR1 (Dolfi et al. 2019), investigate differential source counts (Chen & Schwarz 2015), and by cross-correlating with measurements of the Cosmic Microwave Background, search for the effects of dark energy via the integrated Sachs-Wolfe effect (Sachs & Wolfe 1967). Additionally, GLEAM-X may help to improve sky models for studies of the Epoch of Reionisation, by measuring source brightnesses below 100 MHz, imaging slightly deeper, and separating sources into more components than LoBES (Lynch et al. 2021).

Continuum Galactic science shows promise with MWA Phase II (Tremblay et al. 2022), and given the excellent results from our initial exploration of jointly deconvolving GLEAM and GLEAM-X, we expect to make new detections of supernova remnants (SNRs; see e.g. Hurley-Walker et al. 2019a) and improve

measurements of cosmic ray electrons in the Galactic Plane (following Su et al. 2018). Additionally the improved resolution, sensitivity, and wide bandwidth will make possible the examination of the unshocked ejecta of SNRs (Arias et al. 2018) and interactions with their environments (Castelletti et al. 2021) via measurements of low-frequency thermal absorption. This creates excellent synergy with TeV observations by the High Energy Stereoscopic System (Hinton & HESS Collaboration 2004; Aharonian et al. 2006) and the upcoming Cherenkov Telescope Array (Acharya et al. 2013) to search for sites of cosmic ray acceleration in our Galaxy (e.g. Maxted et al. 2019).

The repeated, overlapping epochs of GLEAM-X and its drift scan observing strategy make it possible to explore radio transients and variability on timescales from seconds to years; comparisons to GLEAM enable a seven-year lever arm. Combining these cadences with the wide bandwidth will enable improved investigation of the startling variability of peaked-spectrum sources found by Ross et al. (2021), and enable distance measurements for dispersion-smeared pulsed transients (Hurley-Walker et al. 2022). As evinced by the latter work, GLEAM-X opens new parameter space in the low-frequency radio sky, and potentially enables further serendipitous discoveries beyond our ability to predict.

References

Acharya, B. S., et al. 2013, APh, 43, 3
Aharonian, F., et al. 2006, ApJ, 636, 777
Arias, M., et al. 2018, A&A, 612, A110

Astropy Collaboration. 2013, A&A, 558, A33
Beardsley, A. P., et al., 2019, PASA, 36, e050
Bertin, E., Mellier, Y., Radovich, M., Missonnier, G., Didelon, P., & Morin, B. 2002, in Astronomical Society of the Pacific Conference Series, Vol. 281, Astronomical Data Analysis Software and Systems XI, ed. D. A. Bohlender, D. Durand, & T. H. Handley, 228
Bock, D. C. J., Large, M. I., & Sadler, E. M. 1999, AJ, 117, 1578
Briggs D. S., 1995, PhD thesis, The New Mexico Institute of Mining and Technology, Socorro, New Mexico, www.aoc.nrao.edu/dissertations/dbriggs/
Callingham, J. R., et al. 2017, ApJ, 836, 174
Castelletti G., Supan L., Peters W. M., & Kassim N. E. 2021, A&A, 653, A62
Chen, S., & Schwarz, D. J., 2015, PhyRvD, 91, 043507
Condon, J. J., Cotton, W. D., Greisen, E. W., Yin, Q. F., Perley, R. A., Taylor, G. B., & Broderick, J. J. 1998, AJ, 115, 1693
de Gasperin, F., et al. 2021, A&A, 648, A104
Dolfi, A., Branchini, E., Bilicki, M., Balaguera-Antolnez, A., Prandoni, I., & Pandit, R. 2019, A&A, 623, A148
Drouart, G., et al. 2020, PASA, 37, e026
Dubois, P. F., Hinsen, K., & Hugunin, J. 1996, ComPhC, 10, 262
Duchesne, S. W., & Johnston-Hollitt, M. 2019, PASA, 36, e016
Duchesne, S. W., Johnston-Hollitt, M., Zhu, Z., Wayth, R. B., & Line, J. L. B. 2020, PASA, 37, e037
Duchesne, S. W., Johnston-Hollitt, M., & Bartalucci, I. 2021, PASA, 38, e053
Eddington, A. S., 1913, MNRAS, 73, 359
For, B. Q., et al. 2018, MNRAS, 480, 2743
Franzen, T. M. O., et al. 2016, MNRAS, 459, 3314
Franzen, T. M. O., Vernstrom, T., Jackson, C. A., Hurley-Walker, N., Ekers, R. D., Heald, G., Seymour, N., & White, S. V. 2019, PASA, 36, e004
Franzen, T. M. O., Hurley-Walker, N., White, S. V., Hancock, P. J., Seymour, N., Kapińska, A. D., Staveley-Smith, L., & Wayth, R. B. 2021a, PASA, 38, e014
Franzen, T. M. O., et al. 2021b, PASA, 38, e041
Galvin, T. J., et al. 2018, MNRAS, 474, 779
Giacintucci, S., Markevitch, M., Johnston-Hollitt, M., Wik, D. R., Wang, Q. H. S., & Clarke, T. E. 2020, ApJ, 891, 1
Hale, C. L., et al. 2021, PASA, 38, e058
Hales, C. A. 2017, AJ, 154, 54
Hancock, P. J., Murphy, T., Gaensler, B. M., Hopkins, A., & Curran, J. R. 2012, MNRAS, 422, 1812
Hancock, P. J., Trott, C. M., & Hurley-Walker, N. 2018, PASA, 35, e011
Harris, C. R., et al. 2020, Natur, 585, 357
Heald, G. H., et al. 2015, A&A, 582, A123
Helmboldt, J. F., & Hurley-Walker, N. 2020, RaSc, 55, e07106
Hinton, J. A., & HESS Collaboration, 2004, NewAR, 48, 331
Hodgson, T., Johnston-Hollitt, M., McKinley, B., Vernstrom, T., & Vacca, V. 2020, PASA, 37, e032
Hogg, D. W., & Turner, E. L. 1998, PASP, 110, 727
Hotan, A. W., et al. 2021, PASA, 38, e009
Hunter, J. D. 2007, CSE, 9, 90
Hurley-Walker, N., & Hancock, P. J. 2018, A&C, 25, 94
Hurley-Walker, N., et al. 2015, MNRAS, 447, 2468
Hurley-Walker, N., et al. 2017, MNRAS, 464, 1146
Hurley-Walker, N., et al. 2019a, PASA, 36, e045
Hurley-Walker, N., et al. 2019b, PASA, 36, e047
Hurley-Walker, N., et al. 2019c, PASA, 36, e048
Hurley-Walker, N., et al. 2022, Natur, 601, 526
Hyman, S. D., Lazio, T. J. W., Kassim, N. E., Ray, P. S., Markwardt, C. B., & Yusef-Zadeh, F. 2005, Natur, 434, 50
Intema, H. T., Jagannathan, P., Mooley, K. P., & Frail D. A. 2017, A&A, 598, A78
Joseph, R. C., Trott, C. M., & Wayth, R. B. 2018, AJ, 156, 285
Kapińska A. D., et al. 2017, ApJ, 838, 68
Kurtzer, G. M., Sochat, V., & Bauer, M. W. 2017, PLoS ONE, 12, e0177459
Lacy, M., et al. 2020, PASP, 132, 035001
Lane, W. M., Cotton, W. D., van Velzen, S., Clarke, T. E., Kassim, N. E., Helmboldt, J. F., Lazio, T. J. W., & Cohen, A. S. 2014, MNRAS, 440, 327
Lenc, E., et al. 2017, PASA, 34, e040

Lenc, E., Murphy, T., Lynch, C. R., Kaplan, D. L., & Zhang S. N. 2018, MNRAS, 478, 2835

Line, J. L. B., et al. 2020, PASA, 37, e027

Loi, S. T., et al. 2015, Geophys. Res. Lett., 42, 3707

Lynch, C. R., et al. 2021, PASA, 38, e057

Mauch, T., Murphy, T., Buttery, H. J., Curran, J., Hunstead, R. W., Piestrzynski, B., Robertson, J. G., & Sadler, E. M. 2003, MNRAS, 342, 1117

Maxted, N. I., et al. 2019, ApJ, 885, 129

McConnell, D., et al. 2020, PASA, 37, e048

McKinley, B., et al. 2022, NatAs, 6, 109

Morgan, J., & Galvin, T. 2021, johnsmorgan/mwa_pb_lookup: Version 1.0, 10.5281/zenodo.5083990, ://doi.org/10.5281/zenodo.5083990

Morgan, J. S., et al. 2018, MNRAS, 473, 2965

Murphy, T., et al. 2017, PASA, 34, e020

Norris, R. P., et al. 2011, PASA, 28, 215

Norris, R. P., et al. 2021, PASA, 38, e046

Offringa, A. R., & Smirnov, O. 2017, MNRAS, 471, 301

Offringa, A. R., van de Gronde, J. J., & Roerdink, J. B. T. M. 2012, A&A, 539, A95

Offringa, A. R., et al. 2014, MNRAS, 444, 606

Offringa, A. R., et al. 2016, MNRAS, 458, 1057

Oliphant, T. E. 2007, CSE, 9, 10

Quici, B., et al. 2021, PASA, 38, e008

Riseley, C. J., et al. 2018, PASA, 35, e043

Riseley, C. J., et al. 2020, PASA, 37, e029

Ross, K., et al. 2021, MNRAS, 501, 6139

Sachs, R. K., & Wolfe, A. M. 1967, ApJ, 147, 73

Sault, R. J., Teuben, P. J., & Wright, M. C. H. 1995, in ASP Conference Series, Vol. 77, Astronomical Data Analysis Software and Systems IV, ed. R. A. Shaw, H. E. Payne, & J. J. E. Hayes, 433 (arXiv:astro-ph/0612759)

Shimwell, T. W., et al. 2017, A&A, 598, A104

Sokolowski, M., et al. 2017, PASA, 34, e062

Stewart, A. J., et al. 2016, MNRAS, 456, 2321

Su, H., et al. 2017, MNRAS, 465, 3163

Su, H., et al. 2018, MNRAS, 479, 4041

Taylor, M. B. 2005, in ASP Conference Series, Vol. 347, Astronomical Data Analysis Software and Systems XIV, ed. P. Shopbell, M. Britton, & R. Ebert, 29

Thompson, A. R., Moran, J. M., & Swenson Jr., G. W. 2001, Interferometry and Synthesis in Radio Astronomy (2nd edn)

Tingay, S. J., et al. 2013, PASA, 30, 7

Tremblay, C. D., Bourke, T. L., Green, J. A., Dickey, J. M., Wong, O. I., & Galvin, T. J. 2022, MNRAS, 510, 593

Varghese, S. S., Obenberger, K. S., Dowell, J., & Taylor, G. B. 2019, ApJ, 874, 151

Virtanen, P., et al. 2020, NM, 17, 261

Wayth, R. B., et al. 2015, PASA, 32, e025

Wayth, R. B., et al. 2018, PASA, 35, e033

White, S. V., et al. 2020a, PASA, 37, e017

White, S. V., et al. 2020b, PASA, 37, e018

Zheng, Q., Johnston-Hollitt, M., Duchesne, S. W., & Li, W. T. 2018, MNRAS, 479, 730

van der Tol, S., Veenboer, B., & Offringa, A. R. 2018, A&A, 616, A27

van Haarlem, M. P., et al. 2013, A&A, 556, A2

A. Observations

Table A.1. GLEAM-X observing summary. The HA and Dec are fixed to the locations shown and the sky drifts past for the observing time shown. Observations typically start just after sunset and stop just before sunrise. The four nights published in this work are shown in bold font. Nights identified as having high ionospheric activity are marked with a "*".

Date	HA	Dec (°)	Observing time (hours)
2018-01-26	0	+20	8.4
2018-01-27*	0	+1	8.6
2018-01-28*	0	−12	8.7
2018-02-01*	0	+20	8.8
2018-02-02*	0	+1	7.3
2018-02-03*	0	−12	5.8
2018-02-04	0	−26	8.7
2018-02-05	0	−40	3.2
2018-02-06	0	−55	3.6
2018-02-07	0	−71	5.7
2018-02-09	+1	−26	8.6
2018-02-10	+1	−12	8.1
2018-02-15*	+1	+1	9.0
2018-02-16	+1	−40	8.9
2018-02-17	+1	+20	7.4
2018-02-18	+1	−55	8.9
2018-02-19	+1	−71	9.0
2018-02-20	0	−26	9.0
2018-02-22	0	−12	8.9
2018-02-28	0	−71	9.1
2018-03-01	0	+1	9.1
2018-03-02	0	−40	8.8
2018-03-03	0	+20	9.0
2018-03-04	0	−55	9.1
2018-03-05	−1	−26	9.1
2018-03-07	−1	−12	9.3
2018-03-10	−1	+1	9.5
2018-03-11	−1	−40	9.5
2018-03-12	−1	+20	9.5
2018-03-13	−1	−55	9.6
2018-03-16*	−1	−71	9.7
2018-05-03	0	−26	10.7
2018-05-04	0	−12	10.6
2018-05-05	0	+1	10.8

Table A.1 Continued.

Date	HA	Dec (°)	Observing time (hours)
2018-05-06	0	−40	10.9
2018-05-07	0	+20	10.9
2018-05-08	0	−55	10.7
2018-05-09	0	−71	10.7
2018-05-10	−1	−26	10.7
2018-05-11	−1	−12	10.8
2018-05-12*	−1	+1	10.7
2018-05-13	−1	−40	10.7
2018-05-14	−1	+20	10.9
2018-05-15	−1	−55	10.9
2018-05-16*	−1	−71	10.8
2018-05-17	+1	−26	10.8
2018-05-18*	+1	−12	11.0
2018-05-19	+1	+1	11.0
2018-05-20	+1	−40	10.9
2018-05-21*	+1	+20	10.7
2018-05-22	+1	−55	10.9
2018-05-23	+1	−71	10.9
2018-05-24*	−1	−71	10.9
2018-05-25	0	−26	10.8
2018-05-26	0	+20	10.9
2018-05-27	0	−12	11.0
2018-05-28	0	+1	10.7
2018-05-29*	0	−40	10.7
2018-05-30	0	−55	10.9
2018-05-31*	0	−71	11.0
2018-06-01	+1	−71	11.1
2018-06-03	0	−26	11.0
2018-06-06*	−1	−26	9.9
2018-06-12*	−1	−12	11.0
2018-06-14	−1	+1	10.4
2018-06-17*	−1	−40	11.1
2019-01-27*	0	+1	6.9
2019-01-28*	0	−12	7.2
2019-02-01*	0	+20	7.3
2019-02-02*	0	+1	7.2
2019-02-03	0	−12	7.1
2019-02-04*	0	+1	7.1
2019-02-05	0	−12	6.8
2019-02-15	+1	+1	9.0

Table A.1 Continued.

Date	HA	Dec (°)	Observing time (hours)
2019-03-16	−1	−71	9.0
2019-05-12*	−1	+1	10.7
2019-05-16*	−1	−71	10.7
2019-05-18*	+1	−12	11.0
2019-05-21*	+1	+20	10.8
2019-05-24*	−1	−71	10.9
2019-05-29*	0	−40	10.7
2019-05-31	0	−71	4.5
2019-06-06*	−1	−26	9.2
2019-06-12*	−1	−12	10.3
2019-06-17*	−1	−40	10.1
2020-09-28*	−1	−71	9.8
2020-09-29	−1	−55	9.3
2020-09-30*	−1	−40	8.2
2020-10-01*	−1	−26	7.8
2020-10-02	−1	−12	7.9
2020-10-03	−1	+1	9.8
2020-10-04*	−1	+20	9.8
2020-10-05	0	−71	9.8
2020-10-06	0	−55	9.8
2020-10-07	0	−40	9.8
2020-10-08	0	−26	9.8
2020-10-09	0	−12	9.6
2020-10-10*	0	+1	8.8
2020-10-11	0	+20	9.8
2020-10-12	0	−71	8.6
2020-10-13	0	−55	8.4
2020-10-14	0	−40	5.6
2020-10-15	0	−26	9.1
2020-10-16	0	−12	9.0
2020-10-17*	0	+1	9.8
2020-10-18	0	+20	9.7
2020-10-19	+1	−71	9.5
2020-10-20	+1	−55	9.5
2020-10-21	+1	−40	9.5
2020-10-22	+1	−26	8.2
2020-10-23	+1	−12	9.5
2020-10-24*	+1	+1	9.5
2020-10-25	+1	+20	8.0
		Total:	1,056.5

B. Catalogue Column Names

Table A.2. Column numbers, names, and units for the catalogue. Source names follow International Astronomical Union naming conventions for co-ordinate-based naming. Background and RMS measurements were performed by BANE (Section 3.7); PSF measurements were performed using in-house software as described in Section 3.6; the fitted spectral index parameters were derived as described in Section 4.4; all other measurements were made using AEGEAN. AEGEAN incorporates a constrained fitting algorithm. Shape parameters with an error of −1 indicate that the reported value is equal to either the upper or lower fitting constraint. The columns with the subscript 'wide' are derived from the 200 MHz wideband image. Subsequently, the subscript indicates the central frequency of the measurement, in MHz. These sub-band measurements are made using the priorised fitting mode of Aegean, where the position and shape of the source are determined from the wideband image, and only the flux density is fitted (see Section 4.1). Note therefore that some columns in the priorised fit do not have error bars, because they are linearly propagated from the wideband image values (e.g. major axis a).

Number	Name	Unit	Description
1	Name	hh:mm:ss+dd:mm:ss	International Astronomical Union name
2	background_wide	Jy beam^{-1}	Background in wideband image
3	local_rms_wide	Jy beam^{-1}	Local RMS in wideband image
4	ra_str	hh:mm:ss	Right ascension
5	dec_str	dd:mm:ss	Declination
6	RAJ2000	°	Right ascension
7	err_RAJ2000	°	Error on RA
8	DEJ2000	°	Declination
9	err_DEJ2000	°	Error on Dec
10	peak_flux_wide	Jy beam^{-1}	Peak flux density in wideband image
11	err_peak_flux_wide	Jy beam^{-1}	Fitting error on peak flux density in wideband image
12	int_flux_wide	Jy	Integrated flux density in wideband image
13	err_int_flux_wide	Jy	Error on integrated flux density in wideband image
14	a_wide	″	Major axis of source in wideband image
15	err_a_wide	″	Error on major axis of source in wideband image
16	b_wide	″	Minor axis of source in wideband image
17	err_b_wide	″	Error on minor axis of source in wideband image
18	pa_wide	°	Postion angle of source in wideband image
19	err_pa_wide	°	Error on position angle of source in wideband image
20	residual_mean_wide	Jy beam^{-1}	Mean of residual after source fitting in wideband image
21	residual_std_wide	Jy beam^{-1}	Standard deviation of residual after source fitting
22	err_abs_flux_pct	%	Percent error in absolute flux scale - all frequencies
23	err_fit_flux_pct	%	Percent error on internal flux scale - all frequencies
24	psf_a_wide	″	Major axis of PSF at location of source in wideband image
25	psf_b_wide	″	Minor axis of PSF at location of source in wideband image
26	psf_pa_wide	°	Position angle of PSF at location of source in wideband image
27	background_076	Jy beam^{-1}	Background at 76 MHz
28	local_rms_076	Jy beam^{-1}	Local RMS at 76 MHz
29	peak_flux_076	Jy beam^{-1}	Peak flux density at 76 MHz
30	err_peak_flux_076	Jy beam^{-1}	Fitting error on peak flux density at 76 MHz
31	int_flux_076	Jy	Integrated flux density at 76 MHz
32	err_int_flux_076	Jy	Fitting error on integrated flux density at 76 MHz
33	a_076	″	Major axis of source at 76 MHz
34	b_076	″	Minor axis of source at 76 MHz
35	pa_076	°	Position angle of source at 76 MHz
36	residual_mean_076	Jy beam^{-1}	Mean of residual after source fitting at 76 MHz
37	residual_std_076	Jy beam^{-1}	Standard deviation of residual after source fitting at 76 MHz

Table A.2. Continued.

Number	Name	Unit	Description
38	psf_a_076	″	Major axis of PSF at location of source at 76 MHz
39	psf_b_076	″	Minor axis of PSF at location of source at 76 MHz
40	psf_pa_076	°	Position angle of PSF at location of source at 76 MHz
41	background_084	Jy beam^{-1}	Background at 84 MHz
42	local_rms_084	Jy beam^{-1}	Local RMS at 84 MHz
43	peak_flux_084	Jy beam^{-1}	Peak flux density at 84 MHz
44	err_peak_flux_084	Jy beam^{-1}	Fitting error on peak flux density at 84 MHz
45	int_flux_084	Jy	Integrated flux density at 84 MHz
46	err_int_flux_084	Jy	Fitting error on integrated flux density at 84 MHz
47	a_084	″	Major axis of source at 84 MHz
48	b_084	″	Minor axis of source at 84 MHz
49	pa_084	°	Position angle of source at 84 MHz
50	residual_mean_084	Jy beam^{-1}	Mean of residual after source fitting at 84 MHz
51	residual_std_084	Jy beam^{-1}	Standard deviation of residual after source fitting at 84 MHz
52	psf_a_084	″	Major axis of PSF at location of source at 84 MHz
53	psf_b_084	″	Minor axis of PSF at location of source at 84 MHz
54	psf_pa_084	°	Position angle of PSF at location of source at 84 MHz
55	background_092	Jy beam^{-1}	Background at 92 MHz
56	local_rms_092	Jy beam^{-1}	Local RMS at 92 MHz
57	peak_flux_092	Jy beam^{-1}	Peak flux density at 92 MHz
58	err_peak_flux_092	Jy beam^{-1}	Fitting error on peak flux density at 92 MHz
59	int_flux_092	Jy	Integrated flux density at 92 MHz
60	err_int_flux_092	Jy	Fitting error on integrated flux density at 92 MHz
61	a_092	″	Major axis of source at 92 MHz
62	b_092	″	Minor axis of source at 92 MHz
63	pa_092	°	Position angle of source at 92 MHz
64	residual_mean_092	Jy beam^{-1}	Mean of residual after source fitting at 92 MHz
65	residual_std_092	Jy beam^{-1}	Standard deviation of residual after source fitting at 92 MHz
66	psf_a_092	″	Major axis of PSF at location of source at 92 MHz
67	psf_b_092	″	Minor axis of PSF at location of source at 92 MHz
68	psf_pa_092	°	Position angle of PSF at location of source at 92 MHz
69	background_099	Jy beam^{-1}	Background at 99 MHz
70	local_rms_099	Jy beam^{-1}	Local RMS at 99 MHz
71	peak_flux_099	Jy beam^{-1}	Peak flux density at 99 MHz
72	err_peak_flux_099	Jy beam^{-1}	Fitting error on peak flux density at 99 MHz
73	int_flux_099	Jy	Integrated flux density at 99 MHz
74	err_int_flux_099	Jy	Fitting error on integrated flux density at 99 MHz
75	a_099	″	Major axis of source at 99 MHz
76	b_099	″	Minor axis of source at 99 MHz
77	pa_099	°	Position angle of source at 99 MHz
78	residual_mean_099	Jy beam^{-1}	Mean of residual after source fitting at 99 MHz
79	residual_std_099	Jy beam^{-1}	Standard deviation of residual after source fitting at 99 MHz
80	psf_a_099	″	Major axis of PSF at location of source at 99 MHz
81	psf_b_099	″	Minor axis of PSF at location of source at 99 MHz
82	psf_pa_099	°	Position angle of PSF at location of source at 99 MHz
83	background_107	Jy beam^{-1}	Background at 107 MHz
84	local_rms_107	Jy beam^{-1}	Local RMS at 107 MHz

Table A.2. Continued.

Number	Name	Unit	Description
85	peak_flux_107	Jy beam^{-1}	Peak flux density at 107 MHz
86	err_peak_flux_107	Jy beam^{-1}	Fitting error on peak flux density at 107 MHz
87	int_flux_107	Jy	Integrated flux density at 107 MHz
88	err_int_flux_107	Jy	Fitting error on integrated flux density at 107 MHz
89	a_107	$''$	Major axis of source at 107 MHz
90	b_107	$''$	Minor axis of source at 107 MHz
91	pa_107	$\circ$	Position angle of source at 107 MHz
92	residual_mean_107	Jy beam^{-1}	Mean of residual after source fitting at 107 MHz
93	residual_std_107	Jy beam^{-1}	Standard deviation of residual after source fitting at 107 MHz
94	psf_a_107	$''$	Major axis of PSF at location of source at 107 MHz
95	psf_b_107	$''$	Minor axis of PSF at location of source at 107 MHz
96	psf_pa_107	$\circ$	Position angle of PSF at location of source at 107 MHz
97	background_115	Jy beam^{-1}	Background at 115 MHz
98	local_rms_115	Jy beam^{-1}	Local RMS at 115 MHz
99	peak_flux_115	Jy beam^{-1}	Peak flux density at 115 MHz
100	err_peak_flux_115	Jy beam^{-1}	Fitting error on peak flux density at 115 MHz
101	int_flux_115	Jy	Integrated flux density at 115 MHz
102	err_int_flux_115	Jy	Fitting error on integrated flux density at 115 MHz
103	a_115	$''$	Major axis of source at 115 MHz
104	b_115	$''$	Minor axis of source at 115 MHz
105	pa_115	$\circ$	Position angle of source at 115 MHz
106	residual_mean_115	Jy beam^{-1}	Mean of residual after source fitting at 115 MHz
107	residual_std_115	Jy beam^{-1}	Standard deviation of residual after source fitting at 115 MHz
108	psf_a_115	$''$	Major axis of PSF at location of source at 115 MHz
109	psf_b_115	$''$	Minor axis of PSF at location of source at 115 MHz
110	psf_pa_115	$\circ$	Position angle of PSF at location of source at 115 MHz
111	background_122	Jy beam^{-1}	Background at 122 MHz
112	local_rms_122	Jy beam^{-1}	Local RMS at 122 MHz
113	peak_flux_122	Jy beam^{-1}	Peak flux density at 122 MHz
114	err_peak_flux_122	Jy beam^{-1}	Fitting error on peak flux density at 122 MHz
115	int_flux_122	Jy	Integrated flux density at 122 MHz
116	err_int_flux_122	Jy	Fitting error on integrated flux density at 122 MHz
117	a_122	$''$	Major axis of source at 122 MHz
118	b_122	$''$	Minor axis of source at 122 MHz
119	pa_122	$\circ$	Position angle of source at 122 MHz
120	residual_mean_122	Jy beam^{-1}	Mean of residual after source fitting at 122 MHz
121	residual_std_122	Jy beam^{-1}	Standard deviation of residual after source fitting at 122 MHz
122	psf_a_122	$''$	Major axis of PSF at location of source at 122 MHz
123	psf_b_122	$''$	Minor axis of PSF at location of source at 122 MHz
124	psf_pa_122	$\circ$	Position angle of PSF at location of source at 122 MHz
125	background_130	Jy beam^{-1}	Background at 130 MHz
126	local_rms_130	Jy beam^{-1}	Local RMS at 130 MHz
127	peak_flux_130	Jy beam^{-1}	Peak flux density at 130 MHz
128	err_peak_flux_130	Jy beam^{-1}	Fitting error on peak flux density at 130 MHz
129	int_flux_130	Jy	Integrated flux density at 130 MHz
130	err_int_flux_130	Jy	Fitting error on integrated flux density at 130 MHz

Table A.2. Continued.

Number	Name	Unit	Description
131	a_130	″	Major axis of source at 130 MHz
132	b_130	″	Minor axis of source at 130 MHz
133	pa_130	°	Position angle of source at 130 MHz
134	residual_mean_130	Jy beam^{-1}	Mean of residual after source fitting at 130 MHz
135	residual_std_130	Jy beam^{-1}	Standard deviation of residual after source fitting at 130 MHz
136	psf_a_130	″	Major axis of PSF at location of source at 130 MHz
137	psf_b_130	″	Minor axis of PSF at location of source at 130 MHz
138	psf_pa_130	°	Position angle of PSF at location of source at 130 MHz
139	background_143	Jy beam^{-1}	Background at 143 MHz
140	local_rms_143	Jy beam^{-1}	Local RMS at 143 MHz
141	peak_flux_143	Jy beam^{-1}	Peak flux density at 143 MHz
142	err_peak_flux_143	Jy beam^{-1}	Fitting error on peak flux density at 143 MHz
143	int_flux_143	Jy	Integrated flux density at 143 MHz
144	err_int_flux_143	Jy	Fitting error on integrated flux density at 143 MHz
145	a_143	″	Major axis of source at 143 MHz
146	b_143	″	Minor axis of source at 143 MHz
147	pa_143	°	Position angle of source at 143 MHz
148	residual_mean_143	Jy beam^{-1}	Mean of residual after source fitting at 143 MHz
149	residual_std_143	Jy beam^{-1}	Standard deviation of residual after source fitting at 143 MHz
150	psf_a_143	″	Major axis of PSF at location of source at 143 MHz
151	psf_b_143	″	Minor axis of PSF at location of source at 143 MHz
152	psf_pa_143	°	Position angle of PSF at location of source at 143 MHz
153	background_151	Jy beam^{-1}	Background at 151 MHz
154	local_rms_151	Jy beam^{-1}	Local RMS at 151 MHz
155	peak_flux_151	Jy beam^{-1}	Peak flux density at 151 MHz
156	err_peak_flux_151	Jy beam^{-1}	Fitting error on peak flux density at 151 MHz
157	int_flux_151	Jy	Integrated flux density at 151 MHz
158	err_int_flux_151	Jy	Fitting error on integrated flux density at 151 MHz
159	a_151	″	Major axis of source at 151 MHz
160	b_151	″	Minor axis of source at 151 MHz
161	pa_151	°	Position angle of source at 151 MHz
162	residual_mean_151	Jy beam^{-1}	Mean of residual after source fitting at 151 MHz
163	residual_std_151	Jy beam^{-1}	Standard deviation of residual after source fitting at 151 MHz
164	psf_a_151	″	Major axis of PSF at location of source at 151 MHz
165	psf_b_151	″	Minor axis of PSF at location of source at 151 MHz
166	psf_pa_151	°	Position angle of PSF at location of source at 151 MHz
167	background_158	Jy beam^{-1}	Background at 158 MHz
168	local_rms_158	Jy beam^{-1}	Local RMS at 158 MHz
169	peak_flux_158	Jy beam^{-1}	Peak flux density at 158 MHz
170	err_peak_flux_158	Jy beam^{-1}	Fitting error on peak flux density at 158 MHz
171	int_flux_158	Jy	Integrated flux density at 158 MHz
172	err_int_flux_158	Jy	Fitting error on integrated flux density at 158 MHz
173	a_158	″	Major axis of source at 158 MHz
174	b_158	″	Minor axis of source at 158 MHz
175	pa_158	°	Position angle of source at 158 MHz
176	residual_mean_158	Jy beam^{-1}	Mean of residual after source fitting at 158 MHz
177	residual_std_158	Jy beam^{-1}	Standard deviation of residual after source fitting at 158 MHz
178	psf_a_158	″	Major axis of PSF at location of source at 158 MHz

Table A.2. Continued.

Number	Name	Unit	Description
179	psf_b_158	″	Minor axis of PSF at location of source at 158 MHz
180	psf_pa_158	°	Position angle of PSF at location of source at 158 MHz
181	background_166	Jy beam^{-1}	Background at 166 MHz
182	local_rms_166	Jy beam^{-1}	Local RMS at 166 MHz
183	peak_flux_166	Jy beam^{-1}	Peak flux density at 166 MHz
184	err_peak_flux_166	Jy beam^{-1}	Fitting error on peak flux density at 166 MHz
185	int_flux_166	Jy	Integrated flux density at 166 MHz
186	err_int_flux_166	Jy	Fitting error on integrated flux density at 166 MHz
187	a_166	″	Major axis of source at 166 MHz
188	b_166	″	Minor axis of source at 166 MHz
189	pa_166	°	Position angle of source at 166 MHz
190	residual_mean_166	Jy beam^{-1}	Mean of residual after source fitting at 166 MHz
191	residual_std_166	Jy beam^{-1}	Standard deviation of residual after source fitting at 166 MHz
192	psf_a_166	″	Major axis of PSF at location of source at 166 MHz
193	psf_b_166	″	Minor axis of PSF at location of source at 166 MHz
194	psf_pa_166	°	Position angle of PSF at location of source at 166 MHz
195	background_174	Jy beam^{-1}	Background at 174 MHz
196	local_rms_174	Jy beam^{-1}	Local RMS at 174 MHz
197	peak_flux_174	Jy beam^{-1}	Peak flux density at 174 MHz
198	err_peak_flux_174	Jy beam^{-1}	Fitting error on peak flux density at 174 MHz
199	int_flux_174	Jy	Integrated flux density at 174 MHz
200	err_int_flux_174	Jy	Fitting error on integrated flux density at 174 MHz
201	a_174	″	Major axis of source at 174 MHz
202	b_174	″	Minor axis of source at 174 MHz
203	pa_174	°	Position angle of source at 174 MHz
204	residual_mean_174	Jy beam^{-1}	Mean of residual after source fitting at 174 MHz
205	residual_std_174	Jy beam^{-1}	Standard deviation of residual after source fitting at 174 MHz
206	psf_a_174	″	Major axis of PSF at location of source at 174 MHz
207	psf_b_174	″	Minor axis of PSF at location of source at 174 MHz
208	psf_pa_174	°	Position angle of PSF at location of source at 174 MHz
209	background_181	Jy beam^{-1}	Background at 181 MHz
210	local_rms_181	Jy beam^{-1}	Local RMS at 181 MHz
211	peak_flux_181	Jy beam^{-1}	Peak flux density at 181 MHz
212	err_peak_flux_181	Jy beam^{-1}	Fitting error on peak flux density at 181 MHz
213	int_flux_181	Jy	Integrated flux density at 181 MHz
214	err_int_flux_181	Jy	Fitting error on integrated flux density at 181 MHz
215	a_181	″	Major axis of source at 181 MHz
216	b_181	″	Minor axis of source at 181 MHz
217	pa_181	°	Position angle of source at 181 MHz
218	residual_mean_181	Jy beam^{-1}	Mean of residual after source fitting at 181 MHz
219	residual_std_181	Jy beam^{-1}	Standard deviation of residual after source fitting at 181 MHz
220	psf_a_181	″	Major axis of PSF at location of source at 181 MHz
221	psf_b_181	″	Minor axis of PSF at location of source at 181 MHz
222	psf_pa_181	°	Position angle of PSF at location of source at 181 MHz
223	background_189	Jy beam^{-1}	Background at 189 MHz
224	local_rms_189	Jy beam^{-1}	Local RMS at 189 MHz
225	peak_flux_189	Jy beam^{-1}	Peak flux density at 189 MHz
226	err_peak_flux_189	Jy beam^{-1}	Fitting error on peak flux density at 189 MHz

Table A.2. Continued.

Number	Name	Unit	Description
227	int_flux_189	Jy	Integrated flux density at 189 MHz
228	err_int_flux_189	Jy	Fitting error on integrated flux density at 189 MHz
229	a_189	$''$	Major axis of source at 189 MHz
230	b_189	$''$	Minor axis of source at 189 MHz
231	pa_189	$\circ$	Position angle of source at 189 MHz
232	residual_mean_189	Jy beam^{-1}	Mean of residual after source fitting at 189 MHz
233	residual_std_189	Jy beam^{-1}	Standard deviation of residual after source fitting at 189 MHz
234	psf_a_189	$''$	Major axis of PSF at location of source at 189 MHz
235	psf_b_189	$''$	Minor axis of PSF at location of source at 189 MHz
236	psf_pa_189	$\circ$	Position angle of PSF at location of source at 189 MHz
237	background_197	Jy beam^{-1}	Background at 197 MHz
238	local_rms_197	Jy beam^{-1}	Local RMS at 197 MHz
239	peak_flux_197	Jy beam^{-1}	Peak flux density at 197 MHz
240	err_peak_flux_197	Jy beam^{-1}	Fitting error on peak flux density at 197 MHz
241	int_flux_197	Jy	Integrated flux density at 197 MHz
242	err_int_flux_197	Jy	Fitting error on integrated flux density at 197 MHz
243	a_197	$''$	Major axis of source at 197 MHz
244	b_197	$''$	Minor axis of source at 197 MHz
245	pa_197	$\circ$	Position angle of source at 197 MHz
246	residual_mean_197	Jy beam^{-1}	Mean of residual after source fitting at 197 MHz
247	residual_std_197	Jy beam^{-1}	Standard deviation of residual after source fitting at 197 MHz
248	psf_a_197	$''$	Major axis of PSF at location of source at 197 MHz
249	psf_b_197	$''$	Minor axis of PSF at location of source at 197 MHz
250	psf_pa_197	$\circ$	Position angle of PSF at location of source at 197 MHz
251	background_204	Jy beam^{-1}	Background at 204 MHz
252	local_rms_204	Jy beam^{-1}	Local RMS at 204 MHz
253	peak_flux_204	Jy beam^{-1}	Peak flux density at 204 MHz
254	err_peak_flux_204	Jy beam^{-1}	Fitting error on peak flux density at 204 MHz
255	int_flux_204	Jy	Integrated flux density at 204 MHz
256	err_int_flux_204	Jy	Fitting error on integrated flux density at 204 MHz
257	a_204	$''$	Major axis of source at 204 MHz
258	b_204	$''$	Minor axis of source at 204 MHz
259	pa_204	$\circ$	Position angle of source at 204 MHz
260	residual_mean_204	Jy beam^{-1}	Mean of residual after source fitting at 204 MHz
261	residual_std_204	Jy beam^{-1}	Standard deviation of residual after source fitting at 204 MHz
262	psf_a_204	$''$	Major axis of PSF at location of source at 204 MHz
263	psf_b_204	$''$	Minor axis of PSF at location of source at 204 MHz
264	psf_pa_204	$\circ$	Position angle of PSF at location of source at 204 MHz
265	background_212	Jy beam^{-1}	Background at 212 MHz
266	local_rms_212	Jy beam^{-1}	Local RMS at 212 MHz
267	peak_flux_212	Jy beam^{-1}	Peak flux density at 212 MHz
268	err_peak_flux_212	Jy beam^{-1}	Fitting error on peak flux density at 212 MHz
269	int_flux_212	Jy	Integrated flux density at 212 MHz
270	err_int_flux_212	Jy	Fitting error on integrated flux density at 212 MHz
271	a_212	$''$	Major axis of source at 212 MHz
272	b_212	$''$	Minor axis of source at 212 MHz
273	pa_212	$\circ$	Position angle of source at 212 MHz
274	residual_mean_212	Jy beam^{-1}	Mean of residual after source fitting at 212 MHz

Table A.2. Continued.

Number	Name	Unit	Description
275	residual_std_212	Jy beam^{-1}	Standard deviation of residual after source fitting at 212 MHz
276	psf_a_212	″	Major axis of PSF at location of source at 212 MHz
277	psf_b_212	″	Minor axis of PSF at location of source at 212 MHz
278	psf_pa_212	°	Position angle of PSF at location of source at 212 MHz
279	background_220	Jy beam^{-1}	Background at 220 MHz
280	local_rms_220	Jy beam^{-1}	Local RMS at 220 MHz
281	peak_flux_220	Jy beam^{-1}	Peak flux density at 220 MHz
282	err_peak_flux_220	Jy beam^{-1}	Fitting error on peak flux density at 220 MHz
283	int_flux_220	Jy	Integrated flux density at 220 MHz
284	err_int_flux_220	Jy	Fitting error on integrated flux density at 220 MHz
285	a_220	″	Major axis of source at 220 MHz
286	b_220	″	Minor axis of source at 220 MHz
287	pa_220	°	Position angle of source at 220 MHz
288	residual_mean_220	Jy beam^{-1}	Mean of residual after source fitting at 220 MHz
289	residual_std_220	Jy beam^{-1}	Standard deviation of residual after source fitting at 220 MHz
290	psf_a_220	″	Major axis of PSF at location of source at 220 MHz
291	psf_b_220	″	Minor axis of PSF at location of source at 220 MHz
292	psf_pa_220	°	Position angle of PSF at location of source at 220 MHz
293	background_227	Jy beam^{-1}	Background at 227 MHz
294	local_rms_227	Jy beam^{-1}	Local RMS at 227 MHz
295	peak_flux_227	Jy beam^{-1}	Peak flux density at 227 MHz
296	err_peak_flux_227	Jy beam^{-1}	Fitting error on peak flux density at 227 MHz
297	int_flux_227	Jy	Integrated flux density at 227 MHz
298	err_int_flux_227	Jy	Fitting error on integrated flux density at 227 MHz
299	a_227	″	Major axis of source at 227 MHz
300	b_227	″	Minor axis of source at 227 MHz
301	pa_227	°	Position angle of source at 227 MHz
302	residual_mean_227	Jy beam^{-1}	Mean of residual after source fitting at 227 MHz
303	residual_std_227	Jy beam^{-1}	Standard deviation of residual after source fitting at 227 MHz
304	psf_a_227	″	Major axis of PSF at location of source at 227 MHz
305	psf_b_227	″	Minor axis of PSF at location of source at 227 MHz
306	psf_pa_227	°	Position angle of PSF at location of source at 227 MHz
307	background_W_087	Jy beam^{-1}	Background at 072-103 MHz
308	local_rms_W_087	Jy beam^{-1}	Local RMS at 072-103 MHz
309	peak_flux_W_087	Jy beam^{-1}	Peak flux density at 072-103 MHz
310	err_peak_flux_W_087	Jy beam^{-1}	Fitting error on peak flux density at 072-103 MHz
311	int_flux_W_087	Jy	Integrated flux density at 072-103 MHz
312	err_int_flux_W_087	Jy	Fitting error on integrated flux density at 072-103 MHz
313	a_W_087	″	Major axis of source at 072-103 MHz
314	b_W_087	″	Minor axis of source at 072-103 MHz
315	pa_W_087	°	Position angle of source at 072-103 MHz
316	residual_mean_W_087	Jy beam^{-1}	Mean of residual after source fitting at 072-103 MHz
317	residual_std_W_087	Jy beam^{-1}	Standard deviation of residual after source fitting at 072-103 MHz
318	psf_a_W_087	″	Major axis of PSF at location of source at 072-103 MHz
319	psf_b_W_087	″	Minor axis of PSF at location of source at 072-103 MHz
320	psf_pa_W_087	°	Position angle of PSF at location of source at 072-103 MHz
321	background_W_118	Jy beam^{-1}	Background at 103-134 MHz
322	local_rms_W_118	Jy beam^{-1}	Local RMS at 103-134 MHz

Table A.2. Continued.

Number	Name	Unit	Description
323	peak_flux_W_118	Jy beam^{-1}	Peak flux density at 103-134 MHz
324	err_peak_flux_W_118	Jy beam^{-1}	Fitting error on peak flux density at 103-134 MHz
325	int_flux_W_118	Jy	Integrated flux density at 103-134 MHz
326	err_int_flux_W_118	Jy	Fitting error on integrated flux density at 103-134 MHz
327	a_W_118	$''$	Major axis of source at 103-134 MHz
328	b_W_118	$''$	Minor axis of source at 103-134 MHz
329	pa_W_118	$\circ$	Position angle of source at 103-134 MHz
330	residual_mean_W_118	Jy beam^{-1}	Mean of residual after source fitting at 103-134 MHz
331	residual_std_W_118	Jy beam^{-1}	Standard deviation of residual after source fitting at 103-134 MHz
332	psf_a_W_118	$''$	Major axis of PSF at location of source at 103-134 MHz
333	psf_b_W_118	$''$	Minor axis of PSF at location of source at 103-134 MHz
334	psf_pa_W_118	$''$	Postion angle of PSF at location of source at 103-134 MHz
335	background_W_154	Jy beam^{-1}	Background at 139-170 MHz
336	local_rms_W_154	Jy beam^{-1}	Local RMS at 139-170 MHz
337	peak_flux_W_154	Jy beam^{-1}	Peak flux density at 139-170 MHz
338	err_peak_flux_W_154	Jy beam^{-1}	Fitting error on peak flux density at 139-170 MHz
339	int_flux_W_154	Jy	Integrated flux density at 139-170 MHz
340	err_int_flux_W_154	Jy	Fitting error on integrated flux density at 139-170 MHz
341	a_W_154	$''$	Major axis of source at 139-170 MHz
342	b_W_154	$''$	Minor axis of source at 139-170 MHz
343	pa_W_154	$\circ$	Position angle of source at 139-170 MHz
344	residual_mean_W_154	Jy beam^{-1}	Mean of residual after source fitting at 139-170 MHz
345	residual_std_W_154	Jy beam^{-1}	Standard deviation of residual after source fitting at 139-170 MHz
346	psf_a_W_154	$''$	Major axis of PSF at location of source at 139-170 MHz
347	psf_b_W_154	$''$	Minor axis of PSF at location of source at 139-170 MHz
348	psf_pa_W_154	$''$	Postion angle of PSF at location of source at 139-170 MHz
349	background_W_185	Jy beam^{-1}	Background at 170-200 MHz
350	local_rms_W_185	Jy beam^{-1}	Local RMS at 170-200 MHz
351	peak_flux_W_185	Jy beam^{-1}	Peak flux density at 170-200 MHz
352	err_peak_flux_W_185	Jy beam^{-1}	Fitting error on peak flux density at 170-200 MHz
353	int_flux_W_185	Jy	Integrated flux density at 170-200 MHz
354	err_int_flux_W_185	Jy	Fitting error on integrated flux density at 170-200 MHz
355	a_W_185	$''$	Major axis of source at 170-200 MHz
356	b_W_185	$''$	Minor axis of source at 170-200 MHz
357	pa_W_185	$\circ$	Position angle of source at 170-200 MHz
358	residual_mean_W_185	Jy beam^{-1}	Mean of residual after source fitting at 170-200 MHz
359	residual_std_W_185	Jy beam^{-1}	Standard deviation of residual after source fitting at 170-200 MHz
360	psf_a_W_185	$''$	Major axis of PSF at location of source at 170-200 MHz
361	psf_b_W_185	$''$	Minor axis of PSF at location of source at 170-200 MHz
362	psf_pa_W_185	$''$	Postion angle of PSF at location of source at 170-200 MHz
363	background_W_215	Jy beam^{-1}	Background at 200-231 MHz
364	local_rms_W_215	Jy beam^{-1}	Local RMS at 200-231 MHz
365	peak_flux_W_215	Jy beam^{-1}	Peak flux density at 200-231 MHz
366	err_peak_flux_W_215	Jy beam^{-1}	Fitting error on peak flux density at 200-231 MHz
367	int_flux_W_215	Jy	Integrated flux density at 200-231 MHz
368	err_int_flux_W_215	Jy	Fitting error on integrated flux density at 200-231 MHz
369	a_W_215	$''$	Major axis of source at 200-231 MHz
370	b_W_215	$''$	Minor axis of source at 200-231 MHz

Table A.2. Continued.

Number	Name	Unit	Description
371	pa_W_215	°	Position angle of source at 200-231 MHz
372	residual_mean_W_215	Jy beam^{-1}	Mean of residual after source fitting at 200-231 MHz
373	residual_std_W_215	Jy beam^{-1}	Standard deviation of residual after source fitting at 200-231 MHz
374	psf_a_W_215	$''$	Major axis of PSF at location of source at 200-231 MHz
375	psf_b_W_215	$''$	Minor axis of PSF at location of source at 200-231 MHz
376	psf_pa_W_215	$''$	Postion angle of PSF at location of source at 200-231 MHz
377	sp_int_flux_fit_200	Jy	Power-law fitted flux density at 200 MHz
378	err_sp_int_flux_fit_200	Jy	Error on power-law fitted flux density at 200 MHz
379	sp_alpha	–	Fitted spectral index assuming a power-law SED
380	err_sp_alpha	–	Error on power-law fitted spectral index
381	sp_reduced_chi2	–	Reduced χ^2 statistic for power-law SED fit
382	csp_int_flux_fit_200	Jy	Curved SED fitted flux density at 200 MHz
383	err_csp_int_flux_fit_200	Jy	Error on curved SED fitted flux density at 200 MHz
384	csp_alpha	–	Fitted spectral index assuming a curved SED
385	err_csp_alpha	–	Error on curved SED fitted spectral index
386	csp_beta	–	Fitted curvature index for curved SED fit
387	err_csp_beta	–	Error on curvature index for curved SED fit
388	csp_reduced_chi2	–	Reduced χ^2 statistic for curved SED fit